ABSTRACT

Title of Document: EMITTANCE MEASUREMENTS OF THE JEFFERSON LAB FREE ELECTRON LASER USING OPTICAL TRANSTION RADIATION

Michael Andrew Holloway, Master of Science, 2007

Directed By: Professor Patrick O'Shea
Department of Electrical and Computer Engineering

Charged particle accelerators, such as the ones that power Free Electron Lasers (FEL), require high quality (low emittance) beams for efficient operation. Accurate and reliable beam diagnostics are essential to monitoring beam parameters in order to maintain a high quality beam. Optical Transition Radiation Interferometry (OTRI) has shown potential to be a quality diagnostic that is especially useful for high brightness electron beams such as Jefferson Labs FEL energy recovery linac. The purpose of this project is to further develop OTRI beam diagnostic techniques. An optical system was designed to make beam size and divergence measurements as well as to prepare for experiments in optical phase space mapping. Beam size and beam divergence measurements were taken to calculate the emittance of the Jefferson Lab FEL. OTRI is also used to separate core and halo beam divergences in order to estimate core and halo emittance separately.

EMITTANCE MEASUREMENTS OF THE JEFFERSON LAB FREE ELECTRON LASER USING OPTICAL TRANSTION RADIATION

By

Michael Andrew Holloway

Thesis submitted to the Faculty of the Graduate School of the
University of Maryland, College Park, in partial fulfillment
of the requirements for the degree of
Master of Science
2007

Advisory Committee:
Professor Patrick O'Shea, Chair
Professor Wesley Lawson
Professor Rami Kishek

Dedication

To my parents, Theodore B. Holloway Jr. and Shirley L. Holloway

Acknowledgements

I would like to first thank Professor Patrick O'Shea, who offered me a job as an undergraduate in his lab and encouraged me to pursue graduate studies. If not for Professor O'Shea I would never have attended graduate school and he has kept me motivated through the tough times.

I would like to give a special thanks to Dr. Ralph Fiorito. Dr. Fiorito has helped me learn what is needed to be done to do quality research. He has gone out of his way to ensure I am successful at my research tasks even though he is not obligated to do so. I would also like to thank the rest of the staff of IREAP who have been good friends and mentors over the last several years.

I like to also thank the entire staff at Jefferson Lab who have given me tremendous support and made me feel welcome. I look forward to working with them in the future.

Table of Contents

List of Tables

.

List of Figures

Chapter 1: Introduction

Today's particle accelerators require high quality beam diagnostics. The ability to accurately measure beam parameters is especially important for accelerators that demand high quality electron beams for efficient operation. The following work is focused on the further development of a diagnostic technique that employs an electromagnetic phenomenon know as transition radiation. The experiments were preformed on the energy recovery linear accelerator (ERL) of the Jefferson Lab Free Electron Laser.

1.1 History and Overview of Transition Radiation Diagnostics

1.1.1 Transition Radiation as a Beam Diagnostic

Transition Radiation (TR) is the burst of radiation that occurs when a charged travels between two media with differing dielectric constants. The first theoretical prediction of transition radiation was made in 1946 by Ginsburg and Frank [1], who derived the spectral angular distribution of transition radiation. The first experimental confirmation of transition radiation did not come until 1959 when Goldsmith and Jelley observed transition radiation created by high energy protons entering a metal surface [2]. Work in the early 1960's provided further experimental confirmation of transition radiation theory. In 1963 Aitken *et al.* captured an image of the angular distribution of transition radiation created when 29 MeV electrons passed through a window of a gas chamber used to detect Cherenkov radiation. From the result, Aiken

et al. suggested the possibility of a using optical transition radiation to measure beam energy [3].

The first major work in the field of Optical Transition Radiation diagnostics occurred during the 1970's with the work of Wartski. Wartski showed that OTR beam images can be used to measure beam intensity profiles. He also showed that the image of the angular distribution of OTR can be used to measure beam energy for relativistic beams [4]. Furthermore, Wartski used OTR from two parallel thin foils to create an interference pattern in the angular distribution image to make highly sensitive beam energy measurements (within 1%) [5].

Investigation into the use of Optical Transition Radiation Interferometry (OTRI) as beam divergence diagnostic began in 1983 [6]. In 1993 R.B Fiorito and D.W. Rule reported successful experiments using OTRI to measure the divergence and emittance on various electron accelerators with energies ranging from 20 MeV - 110 MeV [6]. In recent years, here at the University of Maryland, R.Fiorito and A. Shkvarunets have further developed OTR diagnostics in such ways that include interfering OTR with optical diffraction radiation to measure beam divergence on machines where electron scattering by thin foils would corrupt OTRI measurements [7]. They have also applied OTRI to optically map the transverse phase space of relativistic electron beams [8].

1.1.2 Advantages of Transition Radiation Diagnostics

Transition radiation diagnostics techniques have many advantages over other conventional diagnostics techniques. Some of the key advantages of OTR diagnostics are the following:

1. **Ability of OTR to measure multiple beam parameters**

   OTRI and OTRI have the ability to measure beam size with high resolution and beam divergence, emittance, beam energy, and energy spread with good precision. OTRI can be used to measure RMS divergence and emittances as well as to make localized divergence and trajectory angle measurements (i.e. within the beam spatial distribution) without collimating the beam itself (see section 5.3.3). No other single technique has this range of capabilities.

2. **OTRI uses minimally perturbing thin foil screens**

   OTR and OTRI use thin foils that cause a minimal amount of scattering and disruption of relativistic electron beams.

3. **Single shot data acquisition for beam property measurements**

   A single OTR device can be used to measure multiple parameters simultaneously within a single beam pulse. By comparison, methods such as quadrupole scans and phase space tomography require multiple images to be taken while altering focusing quadrupoles, which can be a lengthy process.

4. **Single position emittance monitoring**

   OTRI can be used to monitor beam size, divergence, and emittance at a single position in the beam line.

5. **Ability to measure multiple beam components**

   Recent experiments, including the one presented in this work, have shown the

potential for OTRI to separate out multiple beam divergence components from the angular distribution pattern of OTRI [8] and measurements of the spatial distribution of the radiation (beam image). The ability to separate beam components could provide the means to measure beam halo properties. Beam halo is low intensity distribution of particles surrounding the core of an intense beam [9]. Beam halo can be a source of beam loss and unwanted radiation due to collisions with the accelerator walls.

Because of their diversity and accuracy, OTR diagnostic techniques are now commonly used in accelerators with energies ranging from tens of keV to tens of GeV .

1.2 Importance of Diagnostics to Free Electron Lasers

Beam quality is absolutely essential for efficient operation of free electron lasers. In order to ensure the beam quality during operation, reliable and accurate measurements are a must. The premium that free electron lasers place on a high quality electron beam is a premiere example of the motivation for the further development of beam diagnostics.

1.2.1 Basic Principles of an FEL

A free electron laser combines accelerator technology with optics. In an FEL, electrons are accelerated up to relativistic energies and sent through an array of permanent magnets with periodically alternating poles called a wiggler. The electrons pass through the wiggler oscillating in periodic fashion emitting a tightly focused beam of light. This process is analogous to spontaneous emission in

conventional laser [10]. The light produced from the electrons is stored in a resonant cavity that bounces the light back and forth through the path of the electron beam in the wiggler. The photon fields in the cavity bunch the electron beam with spacing on the order of a wavelength of the light. This effect give spatial coherence to the light emitted by the electrons and is analogous to stimulated emission in conventional lasers [10]. Figure 1 is a schematic of the Jefferson Lab free electron laser [11].

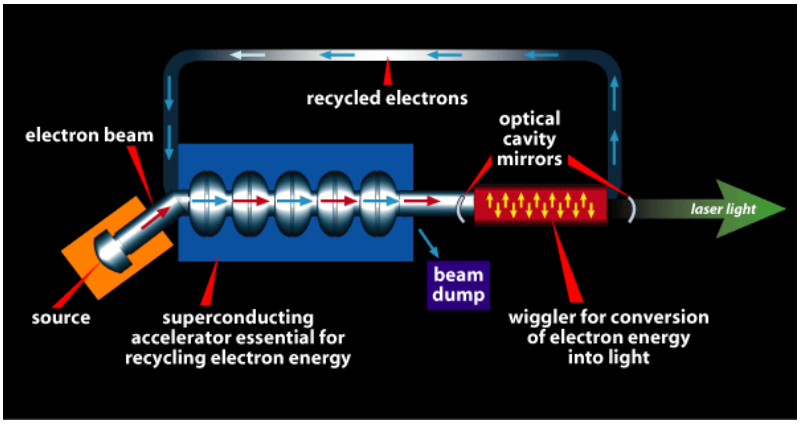

Figure 1: Schematic of a free electron laser

Starting from the left of figure 1, the electrons are emitted from a cathode source and accelerated though a series of super conduction RF cavities. After acceleration, the electrons pass though the wiggler section creating light from their induced oscillations. The optical cavity mirrors store the light and set up the electron photon interaction that modulates the electron beam, which produces gain.

1.2.2 Effect of Emittance on FEL Performance

RMS emittance is an important measure of beam quality in charged particle accelerators. The RMS emittance of a beam is related to the beam size and beam divergence, and provides information on how tightly a beam can be focused and

confined in an accelerator. The lower the lower the emittance, the more tightly focused The gain of an FEL is adversely affected by a high emittance. The single pass gain of the light intensity as the electron beam passes through the wiggler decreases with increasing emittance, so good beam quality is a requirement. In the previous section it was stated that the "stimulated emission" or gain mechanism was the interaction the electrons with the photon field. In order to achieve maximum gain and efficiency, the photon beam must completely overlap the electron beam throughout the wiggler, which can be several meters in length. The electron beam must initially be of high quality, which means it must have a lower divergence and smaller spot size (in other words a lower emittance) than that of the photon beam [10].

1.3 Project Overview

The project details the following accomplishments of my research effort:

- Design of an optical system to make beam divergence measurements using OTRI
- Observation of evidence of two separate beam divergences and spatial distributions from OTRI results
- Development of core-halo model to estimate core and halo emittance separately
- Optics design necessary to carry out future work in optical phase space mapping techniques

Chapter 2: Theoretical Background

2.1 Transition Radiation

2.1.1 General Description

Transition radiation occurs when a charged particle with a constant velocity transitions from a medium of one dielectric constant to a medium with a different dielectric constant [1]. Consider the intersection of two infinite media with differing dielectric constants. As a charged particle travels with uniform motion within the first medium, the particles fields are organized in a manner appropriate to the velocity of the particle and the dielectric properties of the medium. After the particle has passed into the second medium, the particles fields reorganize themselves in a manner appropriate to the dielectric properties of the second medium. As the fields quickly change at the boundary between the two media, some of the field energy is converted into transition radiation [12]. More generally transition radiation occurs anytime a charged particle of uniform motion encounters inhomogeneity in the dielectric properties of the material through which it travels [1].

2.1.2 Relativistic Electrons and a Metal Vacuum Interface

The appropriate theoretical model that applies to the electron beam diagnostic presented in this work is a highly relativistic electron ($\gamma >> 1$) passing from a vacuum to metal and vice versa, since only a metal foil and a mirror are used in the diagnostic apparatus. There are two common models used to conceptualize the radiation process when an electron passes from a vacuum to a metal [13]. One model describes the

process as a collapsing dipole. As the electron approaches the metal at velocity v an image charge is also approaching the surface of the metal from the opposite direction at velocity $-v$. The image charge stops abruptly as it reaches the surface and creates a burst of radiation [13].

Another model uses the idea of virtual quanta. At highly relativistic velocities the electric and magnetic fields of a moving electron are Lorentz contracted. As a result of Lorentz contraction, the electric and magnetic fields of the moving particle are essentially transverse to the direction of motion. Since the magnetic and electric fields are orthogonal to each other and the velocity, the fields are very similar to electromagnetic waves. The Fourier components of the electrons fields are called virtual quanta [14]. Virtual photons will be reflected or refracted as an electron crosses the boundary between media just as real photons would. The reflected or scattered virtual quanta then manifest as transition radiation, which are real photons [14].

In the case of a metal vacuum interface, forward transition radiation is produced close to the direction of the velocity vector of the electron [13]. For a highly relativistic electron, Transition radiation spectral angular density is given by equation

$$\frac{\partial^2 I}{\partial\omega\partial\Omega} = \frac{q^2}{\pi^2 c}\frac{\theta^2}{(\gamma^{-2}+\theta^2)^2} \qquad (1)$$

Where $\theta \sim \gamma^{-1} \ll 1$ [14]. The peak intensity of the transition radiation is centered about the emerging electron at angle $\theta \sim 1/\gamma$ [13]. Backward transition radiation refers to the situation where an electron transitions from a vacuum to a metal [13].

The magnitude and angular distribution of the intensity of the backward transition radiation for a vacuum metal interface is the essentially the same as forward transition radiation. However, for backward TR the intensity distribution is centered on the direction of specular reflection of the incident virtual photons contained in the electron's fields. Figure 2 has an illustration of backward and forward transition radiation.

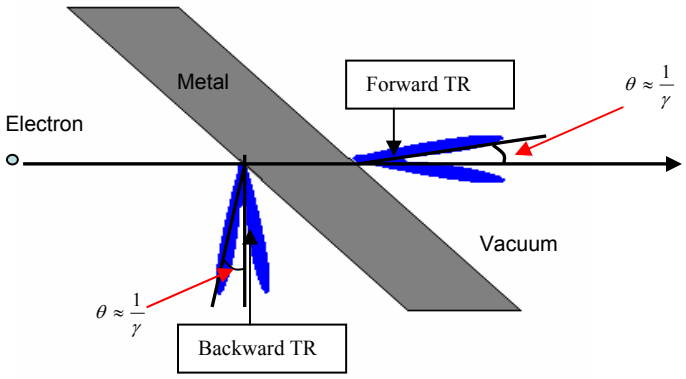

Figure 2: Illustration of backward and forward TR

2.1.3 Characteristics of Transition Radiation

Transition radiation from highly relativistic particles has a high directivity [13]. The peak of transition radiation intensity occurs at the angle $\theta \sim 1/\gamma$ with respect to the velocity vector of the particle for forward transition radiation and the direction of specular reflection for backward transition radiation. For example, the electron beam of Jefferson Lab Free electron Laser has an energy E=115 MeV and $\gamma = 225$. The angular distribution of the intensity of transition radiation has peak intensity at $\theta \approx 4.4$ mrad. The peak intensity, therefore, can be used a beam energy

diagnostic. In addition, the angular distribution is effected by the beam divergence and thus can also be used as a divergence diagnostic. (see Section 2.2)

Another important property of transition radiation is that it is broadband. The upper frequency limit of transition radiation is directly proportional to the energy of the electrons and the plasma frequency of the metal [13]. For high energy particles the upper limit is typically well beyond the visible range [13]. Optical transition radiation or OTR refers to the visible band of the transition radiation spectrum.

2.2 Effect of Beam Divergence on Transition Radiation

If a group of relativistic electrons with sufficiently different trajectory angles impinge on a metal vacuum interface, the intensity distribution of radiation will be measurably different than that of a single electron. For forward OTR each electron will produce radiation with an intensity distribution centered on the velocity vector of each electron. The trajectory angle of each electron will be different. The total intensity of OTR is a superposition of single electron intensity distributions that are all slightly shifted from one another in angle space. Since the OTR has such a high directivity, small shifts in angle space between electrons noticeably affects the measured angular distribution from the ensemble of electrons in the beam [13].

Consider an electron beam of energy 115 MeV with a Gaussian angular distribution of electron trajectory angles is given by equation 2:

$$P(\sigma,\theta)=\left(\frac{1}{2\sigma^2}\right)^{\frac{1}{2}} e^{\frac{-\theta^2}{2\sigma^2}} \qquad (2)$$

where σ is the divergence of the electron beam and θ is the angle of observation. The intensity distribution of OTR is calculated by convolving the angular distribution of

the electron beam with the expression for a single electron OTR intensity distribution in equation (1) [8]. The right side of figure 3 shows the intensity distribution for 3 different divergences of an electron of energy 115 MeV and the left side is the intensity distribution for a single electron for comparison.

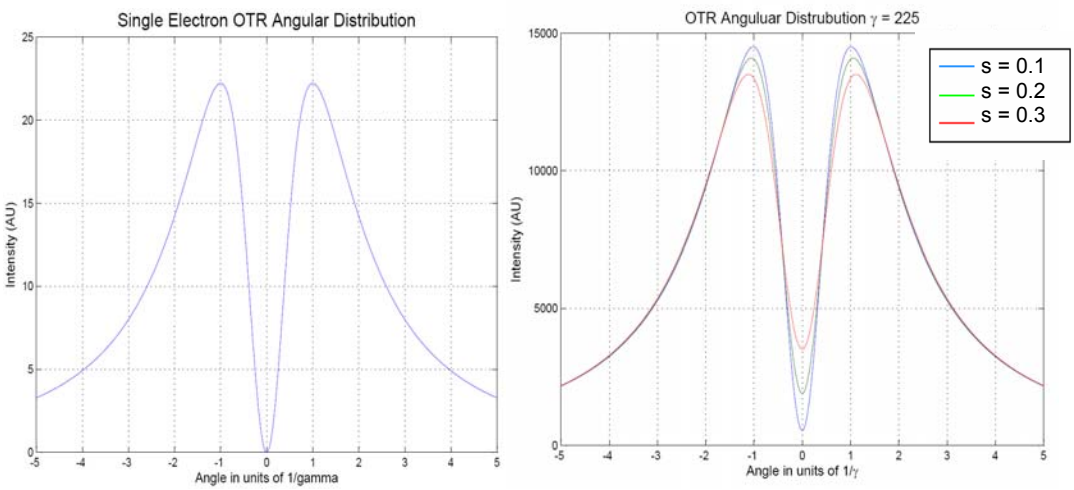

Figure 3: Effect of divergence on single foil OTR

For convenience, both plots are in terms of normalized angle and normalized divergence:

$$\varsigma = \gamma\theta \qquad s = \gamma\sigma \tag{3}$$

The plots show that electron beam divergence has a measurable effect on the intensity of OTR. The divergence can be measured by fitting a calculated intensity profile to a measure intensity profile. The sensitivity of a single OTR foil to measure beam divergence is limited. Observing the plot on the right side of figure 3, normalized divergences below 0.1 would be difficult to measure in practice since the difference between s=0.1 and the plot for a single electron is so small. High quality beams such as the Jefferson Lab free electron laser require a more sensitive diagnostic.

2.3 Optical Transition Radiation Interferometry (OTRI)

2.3.1 Single Electron OTRI

The sensitivity of the OTR angular distribution pattern to divergence can be increased by creating an interference pattern within the single foil intensity profile. The interference pattern is created by using two parallel OTR foils as shown in figure 4 [5].

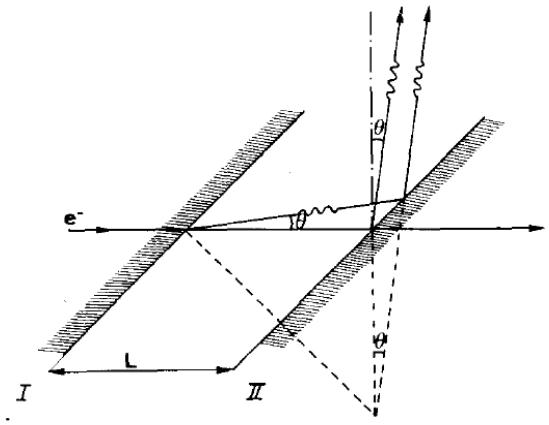

Figure 4: Schematic of two foil OTRI

The forward OTR created at the first foil by an electron interferes with the backward OTR created at foil two. Foil one is typically a very thin metal and foil two is a mirror surface. The intensity distribution for a highly relativistic electron passing though two parallel foils is given by [8]:

$$\frac{\partial^2 I}{\partial\omega\partial\Omega} = \frac{q^2}{\pi^2 c}\frac{\theta^2}{(\gamma^{-2}+\theta^2)^2}\sin^2\left(\frac{\phi}{2}\right) \qquad (4)$$

The expression is the same as the single interface term multiplied by an interference term. The phase difference ϕ is just the phase difference of the light generated at the first foil and the light generated at the second foil and is given by:

$$\phi = \frac{L}{L_v} \tag{5}$$

L is the distance between foils and L_v is the vacuum formation length. The vacuum formation length is defined as [8]:

$$L_v = \frac{\lambda}{\pi\left(\gamma^{-2} + \theta^2\right)} \tag{6}$$

The formation length is the distance at which the electron fields and the photon fields of the generated OTR have sufficiently separated (i.e. differ by pi radians) so that they do not destructively interfere [8]. The inter-foil spacing, L, affects the number of interference fringes that are visible per angular interval. As L increases, so do the number of visible fringes over an angular interval. Figure 5 is plot of the OTRI of a single electron of energy 115 MeV with inter-foil spacing of 47mm and a delta function bandpass filter centered at 650nm.

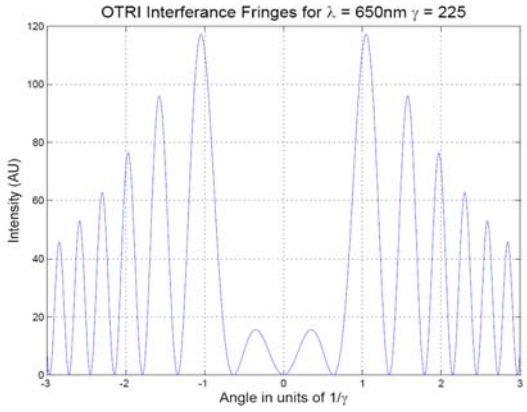

Figure 5: OTRI of a single electron

The value used for the energy, inter-foil spacing and wavelength in the above example and all of the following examples are the expected experimental parameters of the Jefferson Lab Free Electron Laser.

2.3.2 Beam Parameter Effects on Fringe Visibility

Equation 4 shows that OTRI fringe visibility is sensitive to electron beam divergence, energy, and wavelength via the first term, which the angular distribution of single foil OTR, as well as the second term, through the formation length. The first term also serves as an amplitude modulation for the second term, which represents the fringes. Since the first term is a slowly varying function of energy and angle, most of the effect of divergence and energy spread is seen in the second term.

Energy spread is the variation of energy between the electrons within a beam. Since the phase term ϕ of the angular distribution function of OTRI is a function of energy, variations in energy will also have an effect on fringe visibility.

Another factor that affects fringe visibility is the bandwidth of the optical filter used to observe the OTRI interference pattern, since the phase term is ϕ is also a function of wavelength.

The effects of divergence, energy spread, and bandwidth can be roughly estimated by taking the total variation of the phase difference between the OTR in the first foil and the OTR in the second foil. Figure 6 shows two parallel rays of OTR generated by an electron with a trajectory angle θ_e as it passes through two parallel OTR foils spaced d distance apart [15].

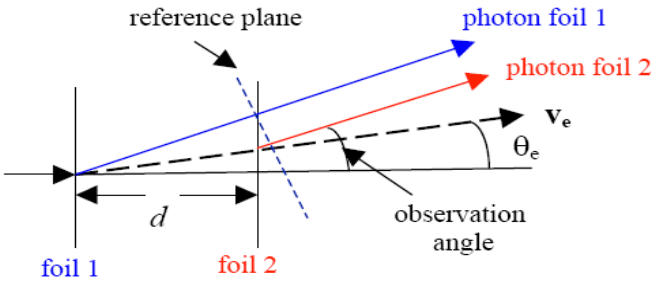

Figure 6: Parallel rays of OTR

The reference plane is perpendicular to the angle of observation θ. The phase difference between photon 1 and photon 2 at the reference plane for $\theta, \theta_e \ll 1$ and $\gamma \gg 1$ is given by:

$$\Delta\psi = \frac{\pi d}{\lambda}\left(\gamma^{-2} + \theta^2 - 2\theta \cdot \theta_e\right) \tag{7}$$

Equation 7 is a more precise definition of the phase since it explicitly shows the effect of the electron angle θ_e. The maximum sensitivity of fringe visibility to either bandwidth ($\delta\lambda$), energy spread ($\delta\gamma$), or normalized divergence (s) occurs when $\delta(\Delta\psi) = \pi$ [15]. The total derivative of the phase difference in terms of normalized divergence and normalized angle with $\delta(\Delta\psi) = \pi$ (equation 3) is:

$$\frac{1}{2}(1+\varsigma^2)\frac{\delta\lambda}{\lambda} + \varsigma s + \frac{\delta\gamma}{\gamma} = \frac{\lambda\gamma^2}{2d} \tag{8}$$

The result above is a useful mathematical tool to approximate the effect of beam parameters on the visibility of OTRI fringes. The goal in designing an interferometer to measure beam divergence is to minimize the effect the bandwidth term and the energy spread term have on fringe visibility.

For experiment at the Jefferson Lab FEL the expected beam parameters are listed in table 1.

Electron beam energy	115 MeV
Energy Spread	2% (2.3 MeV)
RMS Divergence (normalized)	s ~ .05 – .1

Table 1: Expected beam parameters of the Jefferson Lab FEL

Table 2 is the calculated affects of the bandwidth, divergence and energy spread using equation 8 and the expected values of divergence and energy from table 1.

Normalized angle of observation (ζ)	**Effect of bandwidth with $\lambda = 650nm$ and $\delta\lambda = 10nm$ (first term of equation 8)**	**Effect of divergence with s = .05 (second term of equation 8)**	**Effect of enegry spread $\delta\gamma/\gamma$ =2% (third term in equation 8)**
1	0.015385	0.05	0.02
2	0.038462	0.1	0.02
3	0.076923	0.15	0.02
4	0.130769	0.2	0.02

Table 2: Variation of phase terms calculated for JLab FEL parameters

Since the right side of equation 8 is constant, the goal is to have the divergence term dominate the left side of the equation [15]. The results in table 2 shows possible effects from bandwidth at higher angles of observation, and energy spread at lower angles of observation. However, the variation of phase equation remains only an approximation because it does not account for distribution functions of the various parameters (e.g. a Gaussian distribution of beam angles). For the experimental conditions at Jefferson Lab, no definitive conclusion can be drawn from variational analysis since the divergence term does not clearly dominate, but more refined calculations, taking into account distribution functions, reveal that the effect energy spread and filter bandwidth are negligible (section 2.3.4)

2.3.3 The Effect of Divergence on OTRI

Similar to the case with a single OTR foil, the single electron angular distribution function for two foil OTRI in equation 4 is convolved with an electron angular distribution function to observe the effect of electron beam divergence on the interference patterns [8]. Again, a Gaussian electron beam angular distribution is assumed for the as defined in equation 2. Figure 7 is a plot of the of the resulting intensity distribution of OTRI for three different value of electron beam divergence.

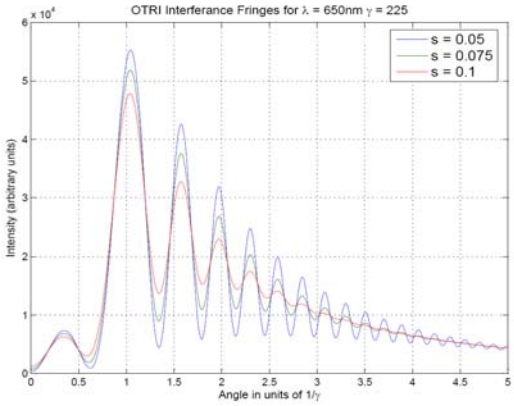

Figure 7: OTRI intensity distribution for 3 divergence values

The range of normalized divergence in the above plot is six times smaller than the range used in the single OTR example in figure 3. The modulation of the interference pattern is significant and measurable despite the small changes in divergence. Figure 7 shows that OTRI is more sensitive to divergence by an order of magnitude compared to single foil OTR in figure 3. The range of divergence used in figure 7 is also the expected range of divergence of the Jefferson Lab FEL 115 MeV ERL.

2.3.4 Simulations Using Convolution Codes

The most precise method for predicting the performance of an OTRI interferometer under various beam conditions is the use of computer codes. The OTRI angular distribution function for a single electron is convolved with model distribution functions for divergence, energy spread, and filter bandwidth. Convolution with multiple distribution functions is an effective method to compare the effects of each of the three parameters. For the purpose of measuring divergence, the goal is to design the interferometer such that energy spread and filter bandwidth have a negligible effect on fringe visibility [8]. The design process involves choosing the necessary inter-foil spacing, wavelength, and bandwidth that produce a useful number of fringes, which are primarily sensitive to beam divergence.

The interferometer used in this experiment has an inter-foil spacing 47mm and the optical filters have a bandwidth of 10nm. Figures 8, 9 and 10 show the result of convolving equation 4 with an appropriate distribution functions for divergence, bandwidth and energy spread.

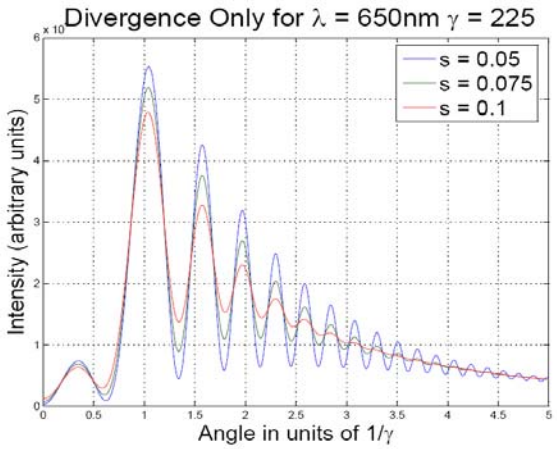

Figure 8: Effect of divergence alone

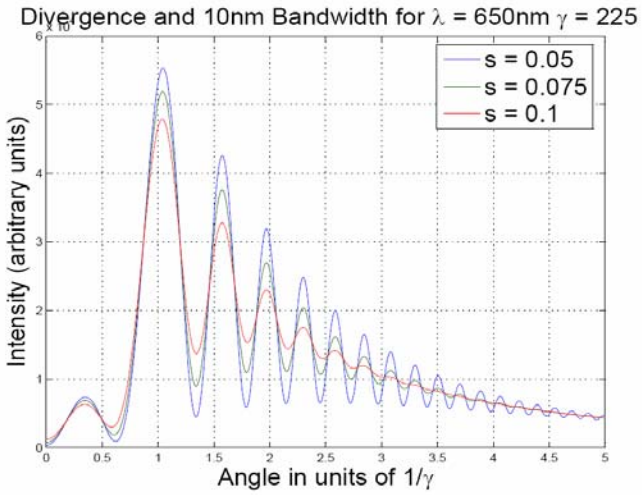

Figure 9: Effect of divergence and bandwidth

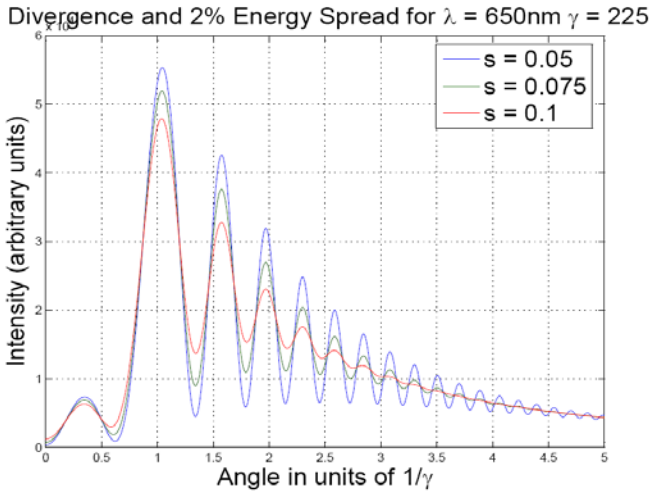

Figure 10: Effect of divergence and energy spread

The distribution functions for divergence and bandwidth are both Gaussian, while energy spread is better modeled as a half cosine function [16] Comparing figure 9 and 10 with figure 8 reveals that energy spread and filter bandwidth have no noticeable effect on the fringe visibility and the fringe visibility is maximally sensitive to the expected range of normalized beam divergence

2.4 Emittance Diagnostics

OTRI does not directly measure the beam emittance but does directly measure the divergence. However, OTRI combined with a simultaneous measure of the beam size can be used to infer the RMS beam emittance when the beam is focused to a waist condition. RMS beam emittance is defined by equation 9 [17]:

$$\tilde{\varepsilon}_x = (\langle x^2 \rangle \langle x'^2 \rangle - \langle xx' \rangle^2)^{\frac{1}{2}} \tag{9}$$

Where $\langle x \rangle$ is the RMS beam size and $\langle x' \rangle$ is the RMS beam divergence. At a beam waist condition the correlation term $\langle xx' \rangle^2$ is zero [17]. The RMS emittance then just reduces to equation 10, which is nothing more the product of the RMS beam size and the RMS divergence.

$$\tilde{\varepsilon}_x = x_{rms} x'_{rms} \tag{10}$$

$$\text{where: } x_{rms} = \sqrt{\langle x^2 \rangle}, \text{ and } x'_{rms} = \sqrt{\langle x'^2 \rangle}$$

Therefore, if a waist condition can be obtained at the interferometer, the emittance of the electron beam can be calculated.

Chapter 3: Experimental Setup

The experimental set up is composed of three parts: 1) an OTR interferometer that intercepts the electron beam and generates an image of the beam and creates the necessary interference pattern used to measure the electron beam divergence. 2) Optics that transport the beam image and angular distribution pattern to their appropriate cameras while preserving the proper fields of view. 3) Two cameras capture the beam image and angular distribution image, which are digitized and store on computer media for quantitative analysis.

3.1 Interferometer

3.1.1 Interferometer Geometry

The two foil interferometer used in this experimental arrangement is shown in the figure 11 [8].

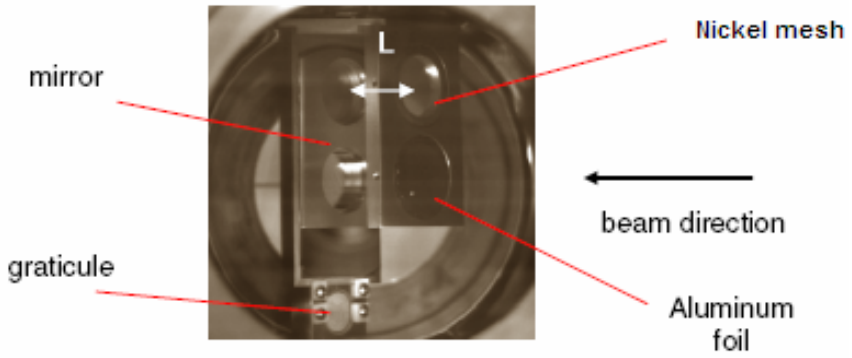

Figure 11: OTRI interferometer assembly

The front face of the interferometer is constructed of aluminum and contains two circular holes that hold OTR foil mounting rings. The bottom mounting ring contains an aluminum foil 0.7 μm thick and the top ring contains a nickel micromesh

5μm thick. The nickel micromesh has square holes 11.2 μm in width that are spaced with a period of 16.9 μm. The back surface is an aluminum frame holding a silicon substrate coated with aluminum to a thickness of 1000 Å for high reflectivity. The silicon mirror surface is parallel to the front surface holding the OTR foils. At the bottom of the silicon mirror is a 19 mm circular optical graticule. The graticule is comprised of a vapor deposited aluminized metric crosshair on a 1mm thick glass substrate. The graticule crosshair has 10 major divisions on each axis. Each division is 0.5mm in length. The distance between the front faces of the foil and mesh and the silicon mirror surface (L) is 47 mm, which is 1.8 formation lengths for a 115 MeV at zero observation angle and a wavelength of 650 nm (see equation 6 in chapter 2) electron beam [8].

3.1.2 Interferometer Beam Line Positioning

The interferometer is suspended in a 6 port cross by a linear actuator whose maximum travel distance is 6 inches, and is oriented at a 45 degree angle with respect to the electron beam direction. Figure 12 is an overhead view of the arrangement.

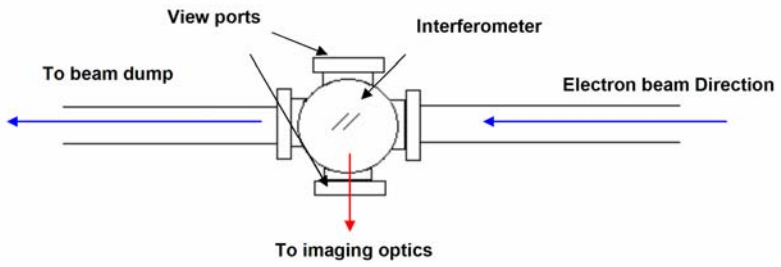

Figure 12: Overhead view of cross containing the interferometer

The two view ports in figure 12 are gold tinted fused silica windows four inches in diameter. The top view port in the figure has a viewer camera attached in order to

monitor the position of the interferometer from a control location. The generated OTR is directed out the bottom view port. The cross is located just before a beam dump in energy recovery linac of the Jefferson Lab FEL as shown in figure 13 [11]. During an experimental run, the electron beam is sent straight through the interferometer to the beam dump instead of steering around the path marked by the black arrows in figure 13 [11]. This position was chosen so the OTRI experiments would not interfere with normal operation of the FEL.

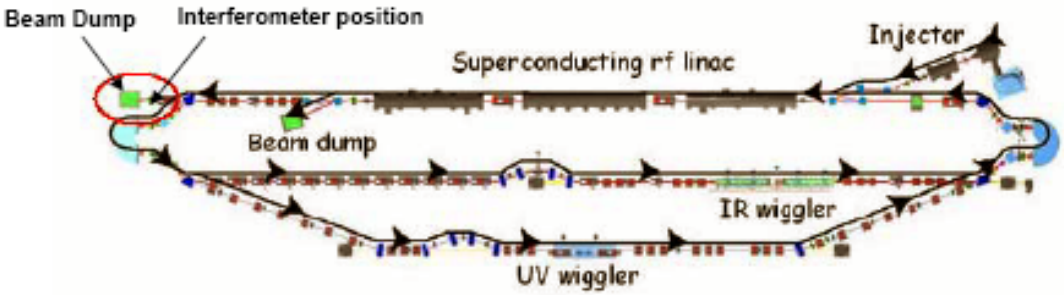

Figure 13: Jefferson Lab FEL ERL

3.1.3 Interferometer Operation and Control

The linear actuator, from which the interferometer is suspended, is remotely operated from FEL control room. The interferometer has four operational positions with respect to the electron beam path, and can also be totally retracted from the beam path.

Starting from the top of the interferometer in figure 11, the first position places the nickel micromesh and the top portion of the silicon mirror in the beam path. This position was used for optics alignment and field of view calibration (section 3.2.3 and 3.2.4).

The second position down the ladder puts the aluminum foil and a portion of the silicon mirror in the beam path. The second position is used to conduct OTRI measurements. The forward generated OTR emitted from the thin aluminum and the backward directed OTR emitted from the mirror surface combine to create the angular distribution interference pattern necessary to measure the electron beam divergence. A camera is focused on the surface of the mirror in order to capture the beam image created by the OTR light. The beam image is used to calculate the RMS beam size.

The third position places only the bottom portion of the silicon mirror in the beam path, leaving the entire front surface clear of the electron beam. The third position can be used to conduct single foil OTR measurements or to simply image the beam.

The last position is the graticule. The graticule is seated such that the surface is flush with the mirror surface. The graticule is used as focusing tool for the imaging optics and beam imaging camera. Since the surface of the graticule is in the same plane as the silicon mirror, illuminating the aluminum crosshair with a laser or other source provides a sharp image to focus a camera precisely at the mirror surface for beam image acquisition. The precise grading of the crosshair provides and accurate means to calibrate the beam imaging camera.

3.2 Optics

3.2.1 Basic Concept

The basic objective of the optics layout is to simultaneously transport two different images to cameras for acquisition. Figure 14 is a schematic of a simple optics arrangement that simultaneously images the beam itself and the far field angular distribution of the OTR produced at the interferometer.

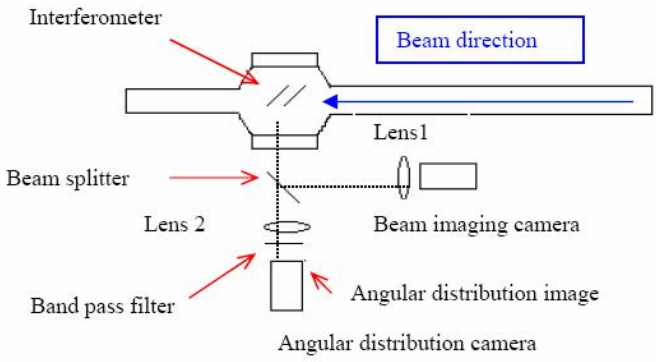

Figure 14: Optics schematic

From the schematic, lens 1 focuses the beam imaging camera to the surface of the silicon mirror. If a pellicle beam splitter with 90% transmission is used, the majority of the OTR passes through the beam splitter and into lens 2. Lens 2 creates an image of the angular distribution (AD) of the OTR in the focal plane of the lens. Figure 15 demonstrates how the AD image is created.

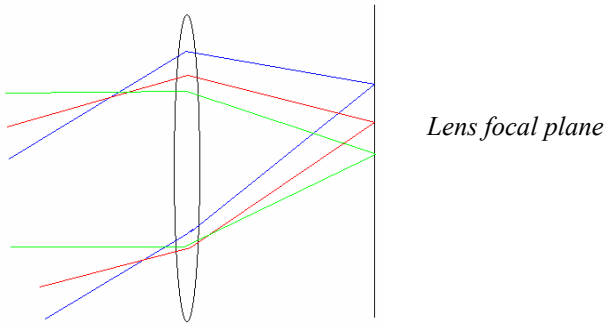

Figure 15: Creation of AD image

All light rays passing through a lens at the same angle will focus to the same spot in the focal plane of the lens, provided the source is more than a focal distance from the lens [18]. The sensor of the far field camera is placed in the focal plane of lens 2, which makes the far field camera focused to the OTR angular distribution pattern.

3.2.2 Optics Design

The optics used in these experiments are designed to achieve the goals described in the previous section, *i.e.* to simultaneously image the beam and its AD. However, there are two factors that increase the complexity of the final design: 1) The cameras need to be shielded from the radiation created at the beam dump 2) The optics are designed in order to carry out future experiments in optical phase space mapping which requires a magnification of the image at a secondary focus.

The optics are arranged on a 2' X 4' optical breadboard table, which is leveled to the beam line. Figure 16 is an overhead view of the optics table.

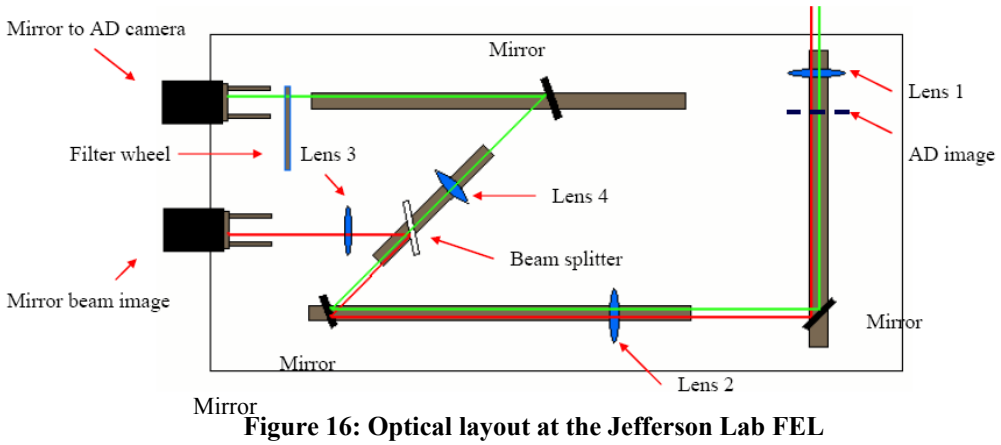

Figure 16: Optical layout at the Jefferson Lab FEL

The green and red lines represent the far field light path and the near field light path respectively.

Lens 1 has a focal length of 200 mm and lens 2 has a focal length of 100 mm. Lens 1 and 2 are spaced 720 mm apart, and together create a ten times magnified beam image from the surface of the silicon mirror of the interferometer to the beam splitter. The AD image is created at the focal plane of lens 1. Lens 3 has a focal length of 400 mm and transports the beam image to the beam imaging camera while lens 4, also with a focal length of 400 mm, relays the AD image to the AD camera. The filter wheel rotates a 650 nm X 10 nm band pass filter, a 450 nm X 10 nm, or a clear aperture in the angular distribution light path.

The purpose of the ten times magnified intermediate beam image at the beam splitter is to carry out future phase space mapping experiments. In optical phase space mapping (OPSM) experiments, the beam splitter will be replaced with an optical mask, which will be used to measure localized divergence of the electron beam within the spatial distribution of the beam image. With a magnified beam image of about 1 cm, a 1mm pinhole can be positioned to allow light from a specific part of the beam

to pass through to the far field camera while the rest of the light is directed to the near field camera. The 10:1 magnification will allow ten or more data points to be taken within the area of the beam image. Further details about future experiments in phase space mapping are described in section 5.3.

The beam dump is very close to the experimental setup and is a source high energy x-ray radiation. The cameras must be shielded with lead to reduce the image noise produced by radiation and protect the CCD cameras from damage. To make shielding the camera easier, both are placed near the floor. The light from both image paths is directed toward the floor by the two mirrors shown on the far left of figure 16. Figure 17 is a side view of the light paths directed down from the optics table to both cameras. Len 5 has a focal length 200 mm and lens 6 is a standard camera lens with focal length 100 mm.

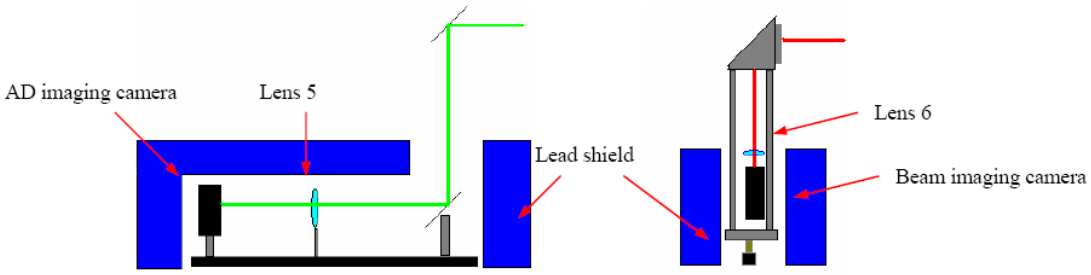

Figure 17: Side view of light path to imaging cameras

Lenses 1 – 5 are all achromats lenses and lens six is a standard fixed focal length camera lens. Achromats are necessary to minimize spherical and chromatic aberration. The entire optical system is designed to ensure an acceptance angle of $10/\gamma$. From the simulation in chapter 2 it was shown the expected interference fringes die out at an angle of about $5/\gamma$. Maintaining an acceptance angle of $10/\gamma$

throughout the entire optics system will ensure that no data is lost in the trip from interferometer to the imaging cameras.

Ray transfer matrices were used to calculate the size of the light ray bundle throughout the entire optical path. Using thin lens approximations, ray transfer matrices can be used calculate the height from the optical axis and angle with respect to the optical axis of a light ray at any point in an optical system with a given input height and angle [19]. The largest electron beam radius expected at the interferometer is about 1 mm [20]. The height and angle of the ray is then checked at the surface of every lens in the entire system to ensure the lens will capture the ray. Figure 18 is a schematic of the process.

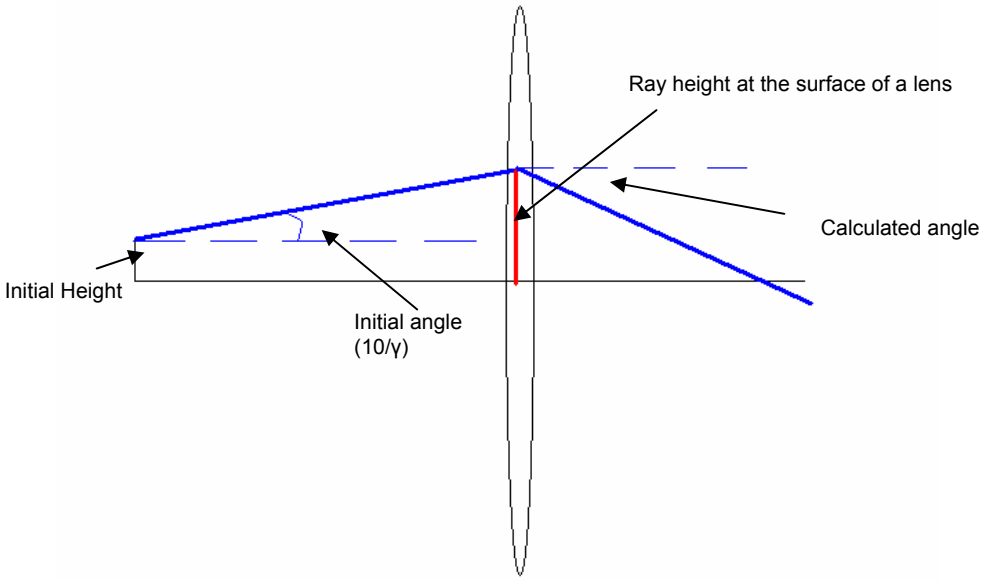

Figure 18: Schematic of ray tracing calculation

The same calculation is performed for the next lens surface in the optics train using the new height and angle at the first lens. The same process is repeated until the

surface of the camera sensor is reached. Figure 19 is the plot of the results of ray transfer matrix calculations performed in Matlab for both the far field and near field beam paths.

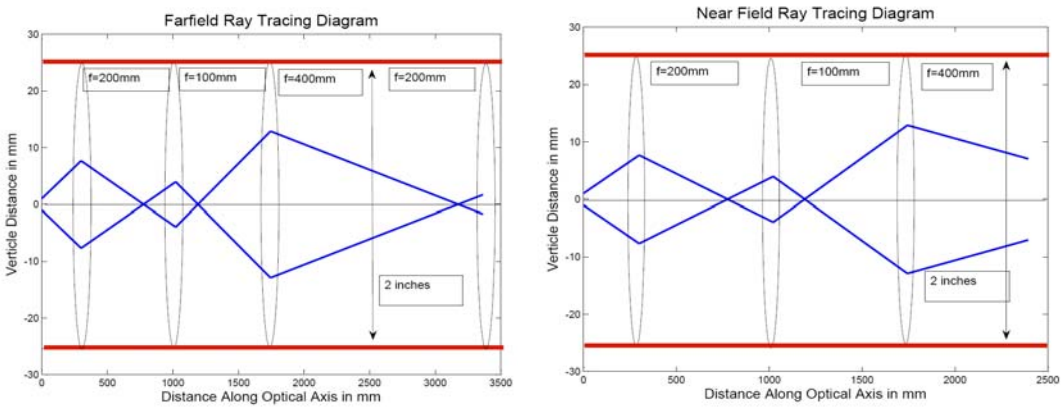

Figure 19: Ray tracing plots for the near field and far field optical path

The initial rays shown in blue start at height of 1mm from the optical axis and has angle of $10/\gamma$ with respect to the optical axis. The minimum aperture in the optics system is 2 inches in diameter and is represented by the red lines on the figure.

3.2.3 Optical Alignment

Good optical alignment is essential to ensure the OTR light travels down the optical axis of the entire optics system. To align the optics a HeNe laser presently installed at Jefferson Lab is used. The laser beam travels down the full length of the linac through the beam pipe along the electron beam path. The laser spot is about 3/4 an inch in diameter when it reaches the interferometer. The interferometer is adjusted so that the nickel mesh position is in the beam path. When the laser strikes the nickel mesh a diffraction pattern is created and reflected off the silicon mirror into the optical system. The diffraction pattern consists of a rectangular pattern of spots with

the central spot containing light at an angle of zero degrees with respect to the electron beam axis. The central order of the diffraction pattern serves as a reference spot to align the optics. In this procedure, the lenses are initially removed. The mirrors are adjust so the central order laser beamlet travels along both the near field and far field beam paths at a constant height. Each lens is the placed in its proper location and adjusted so that the laser spot travels through the center of the lens.

3.2.4 Near Field Focusing and Calibration

To focus the near field camera to the surface of the mirror surface of the interferometer, the interferometer is moved to the graticule position. The HeNe laser described in the previous section illuminates the graticule and creates a focusing image. Referring back to figure 16, lens 1 and 2 are adjusted to focus the image, which is visible to the naked eye, to the beam splitter, and lens 6 is adjusted to focus the near field camera to the surface of the beam splitter. Figure 20 is a frame capture of the graticule image taken from the beam imaging camera.

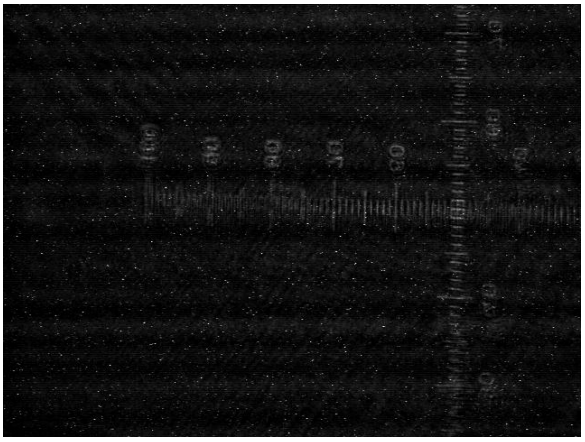

Figure 20: Near field calibration image

The horizontal axis is compressed due to the tilt of the interferometer. Calibration is achieved by measuring the number of pixels per division of the crosshair.

3.2.4 Far Field Focusing and Calibration

The far field camera is focused using the diffraction pattern created by the nickel mesh described in section 3.2.3. Lens 4 and 5 are adjusted till the diffraction spots are at their sharpest in the far field camera. Figure 21 is the image of the diffraction pattern taken from the far field camera.

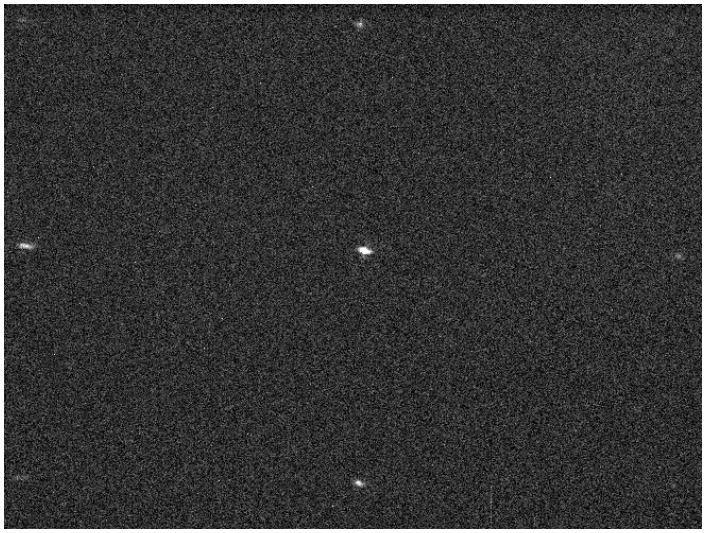

Figure 21: Diffraction pattern image from far field camera

The calibration and angular field of view are determined by calculating the angular position of the first order diffraction spots located directly horizontal and vertical from the central order. Each spot is at an angular position $\theta = \lambda / d$ where $\lambda = 632$ nm is the wavelength of the laser and d = 16.9 μm is the period of the micromesh [8]. Dividing the angular spacing of the first order spots by the number of pixels between the central order and the first order give the calibration. The tilt of the interferometer makes the period in the horizontal direction shorter by a factor of $\sqrt{2}$, and is the

reason why the horizontal first order spots are a greater distance from the central order than the vertical spots.

Calculating the field of view is important to ensure there are enough pixels to resolve each interference fringe. The angular field of view in the vertical direction of figure 10 is about $15/\gamma$. Simulations in chapter 2 show that about 6 fringes are expected out to a distance of $3/\gamma$. The total number of pixels in a vertical line is 510. 6 fringes cover 1/5 of the pixels in the vertical direction, which leaves an acceptable 17 pixels per fringe.

3.3 Imaging Cameras

The near field camera is a standard RS-170 video CCD camera used by the Jefferson Lab FEL group to monitor the electron beam throughout the system. The camera feed is attached to a 10 bit frame grabber and image acquisition is synchronized to the drive laser pulse of the electron gun. As shown in figure 7, lead surrounds the camera to reduce radiation noise and to protect the sensor from damage.

The far field camera is a highly sensitive 16 bit digital cooled CCD camera (SBIG model ST-402ME). The CCD sensor array consists of 765 x 510, 9 microns square pixels. The camera is computer controlled and acquires single images over a specified integration time. The exposure time is controlled by a mechanical shutter and allows integration times from 0.04 to 3600 seconds. The images are downloaded via a USB 2 link. The SBIG camera must be heavily shielded from radiation in all direction due to its sensitivity and cost. Lead bricks completely enclose the camera with at least 4 inches of lead.

Chapter 4: Experimental Results

The following chapter presents the data gathered from OTRI measurements performed at the Jefferson Lab FEL. The beam conditions during data acquisition are listed in table 3.

Beam Energy	115 MeV
Macro Pulse Width	100μs
Micro Pulse rep rate	2MHz
Charge per bunch	135 pC
Beam Current (Avg)	~150μA

Table 3: Electron beam experimental conditions

The beam was separately focused to vertical and horizontal minima (waists), and data was acquired for each waist condition using both 650 x 10 nm and 450 x 10 nm filters. Beam size and beam divergence measurements were performed for each focused waist condition.

4.1 Beam Divergence Measurement

Far field images obtained from the SBIG camera are saved as 16 bit .FIT files. The FIT file format is the international standard for astronomical images [21]. The analysis software used to measure the beam divergence only accepts 8 bit bitmaps and therefore all the images are converted from 16 bit to 8 bit. Close examination of line scans of the interference pattern show that no data is lost in the conversion. For each far field image an intensity profile is needed in order to fit theoretical line scans to those measured from the interference patterns. Beam divergence is determined from the best fit to the data scan.

4.1.1 Data Preparation

A horizontal and vertical sector scan of the intensity profile is made for each far field image. Figure 22 shows the positioning of a sector used to average the intensity for a horizontal line scan.

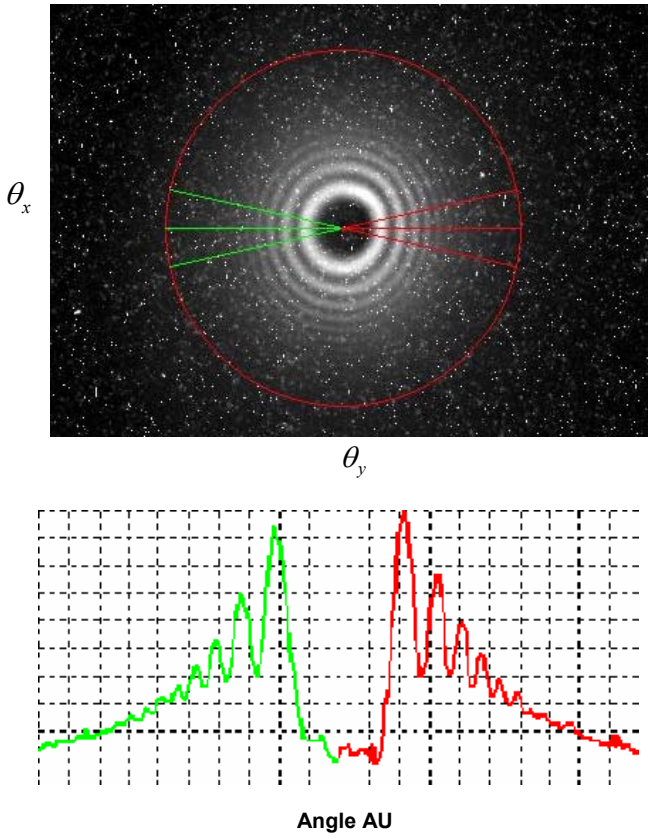

Figure 22: Demonstration of a sector scan

Within the sector, the pixel values along the same radius from the center of the interference pattern are averaged and an averaged intensity value is assigned for each pixel in the direction of the scan. Averaging the pixel values reduces the effect of noise within the data and provides a smoother curve to perform the fit. Care is taken

to minimize the sector angle so that the sector scan is not significantly different than a single line scan through the center of the sector [8].

4.1.2 Data Fitting Procedure

A convolution code similar to the one described in the simulation in chapter 2 is used to produce a theoretical line scan to fit the data. The code plots both the theoretical line scan and the sector averaged line scan of the data curve on the same plot. Many parameters can be adjusted within the code in order to make an accurate fit [8].

First, the following known beam parameters and experimental factors are entered into the code: Beam energy, energy spread, inter-foil spacing, and filter wavelength and bandwidth. The primary objective of the code is to convolve a 2 dimensional electron angular distribution function with the single electron OTRI angular distribution function. The electron angular distribution function can have up 3 Gaussian components each with separate x and y component. Each Gaussian component can be weighted with respect the other components. The variance of each of the Gaussian components provides a corresponding divergence for that component [8].

To perform the fit, sector scans are taken of both the horizontal and vertical components (θ_x and θ_y components) for a given far field picture. The convolution code calculates horizontal (x) and vertical (y) line scans obtained from the 2 D convolution of the single electron intensity over (x, y) angles as well as energy and bandwidth convolutions to produce a theoretical function, which is then fitted to the horizontal and vertical sector averaged line scans obtained from the data. The

theoretical function is given initial guesses for the variance of the x and y components of the divergence and the x variance, y variance and weight of each Gaussian component of the theoretical function is varied manually until the best fit is reached. The best fit is achieved by minimizing the RMS deviation between the calculated curve and the data. The RMS deviation is defined as [8]:

$$D(A) = \frac{1}{(\theta_2 - \theta_1)} \left[\int_{\theta_1}^{\theta_2} \left(\frac{A \cdot E(\theta) - T(\theta)}{A \cdot E(\theta) + T(\theta)} \right)^2 \right]^{\frac{1}{2}} \qquad (11)$$

where $T(\theta)$ is the value of the calculated curve, $E(\theta)$ is the value of the experimental curve and A is and arbitrary scaling constant. The computer code varies A until $D(A)$ is minimized each time $D(A)$ is calculated [3]. $D(A)$ gives an overall view of the uncertainty that occurs between the total fitted function and the data. The error of each divergence is estimated by varying the divergence by small amounts and gauging the sensitivity of $D(A)$ to the small changes. The range of the divergence over which $D(A)$ does not significantly change gives an estimate of the uncertainty.

Interestingly, in all the data acquired from the Jefferson Lab experiments, a proper fit could not be achieved using only a single two dimensional Gaussian component. If the divergence is adjusted to fit the lower order interference fringes, the higher order fringes wash out. Conversely, if the divergence is adjusted so that the interference pattern fits the higher order fringes, the lower order fringes are too large and do not wash out enough. The plots in figure 23 illustrate the attempt to fit a theoretical curve to the interference fringes from the x waist condition of the Jefferson Lab beam using only one angular Gaussian component.

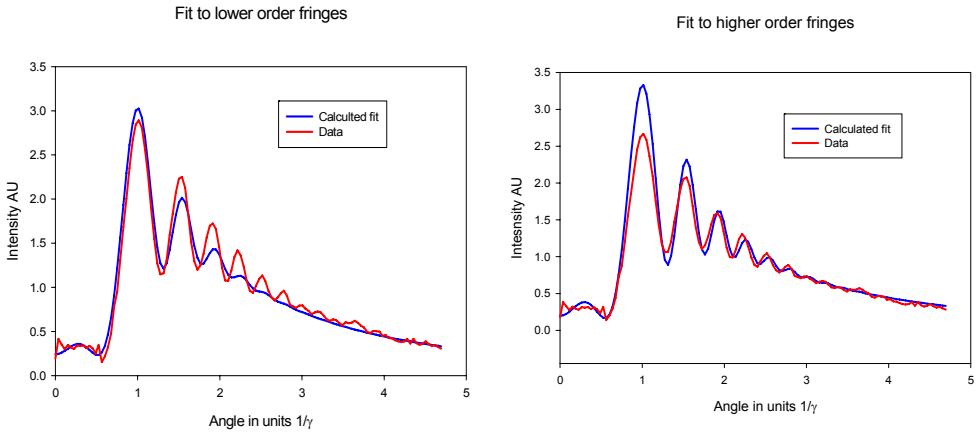

Figure 23: Attempt to fit data using a single component

The only way to get a proper fit to the data is to add a second two dimensional Gaussian component to the theoretical fitting function. The fits for the data presented below were acquired by adjust the divergence as well as the weight of each of the two Gaussian components. This result gives strong evidence that there is a second group of electrons within the beam with a higher divergence than the first component. The second component is present in all the OTRI far field images, which also confirms that there two angular distributions physically present within the electron beam. Similar bimodal distributions have been observed in OTRI experiments at the Brookhaven Accelerator Test Facility (50 MeV linac) and the 95 MeV linac at the Naval Post Graduate School [8].

4.1.3 Experimental Results for Beam Divergence Measurement

The following plots are the data fits for each waist condition at both $\lambda =$ 650nm and $\lambda = 450$nm. The images were taken with a 90s integration time. The two divergence components are labeled $\sigma 1$ and $\sigma 2$ Included below is data from y scans of the x waist. In near field images shown in section 4.3.3, the vertical component at the

x waist looks very similar to the y waist. The beam tune used to obtain the x waist may also be a simultaneous x and y waist. The vertical component of the x waist images are also evaluated for comparison to the y waist. Following the plots is table 2 summarizing the results. The table provides the measured divergence of each component, the percent of the current contribution (or percent of the total number of electrons) resulting from the weight of each angular Gaussian component, and the value D(A) in percent when he beast fit was achieved.

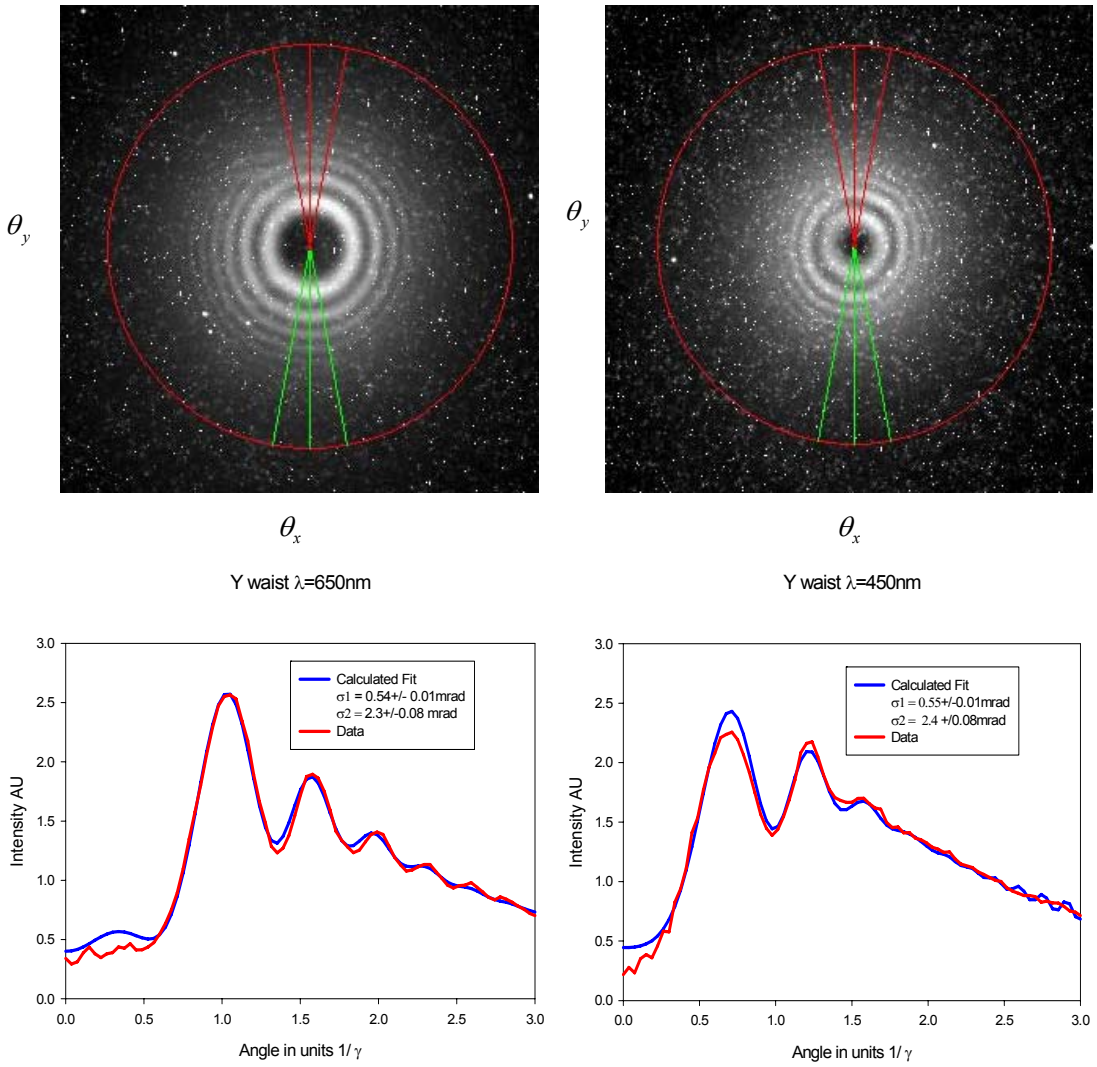

Figure 24: Y divergence measurement for Y waist condition

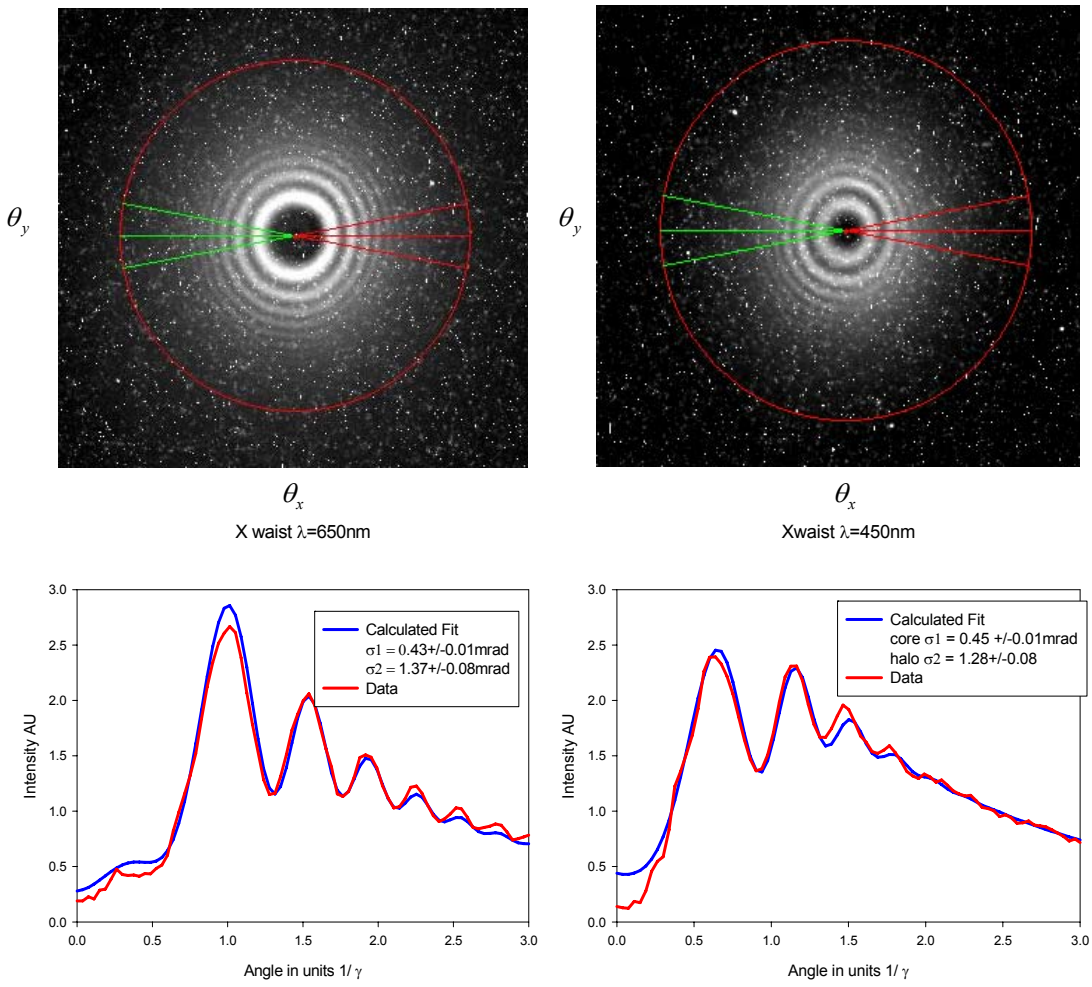

Figure 25: X divergence for X waist condition

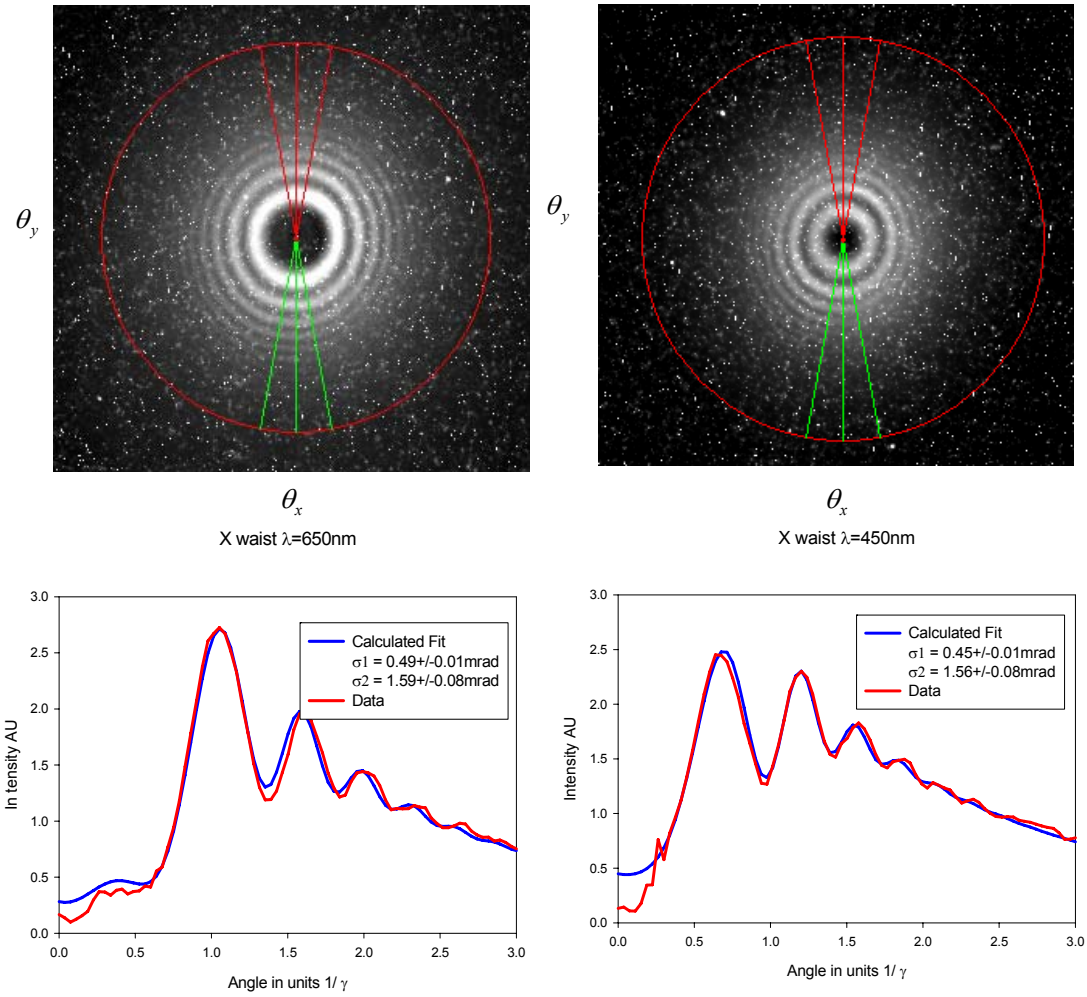

Figure 26: Y divergence measurement at an X waist

Waist	λ (nm)	σ1 (mrad)	σ2 (mrad)	% Current σ1	% Current σ2	D(A)
Y	650	0.54+/-0.01	2.3+/-0.1	68.9 %	31.1 %	3.23%
Y	450	0.55+/-0.01	2.4+/-0.08	69.9%	30.1%	4.25%
X	650	0.43+/-0.01	1.37+/-0.08	67.1%	32.9%	5.42%
X	450	0.45+/-0.01	1.28+/-0.07	67.6%	32.4%	5.39%
X(y scan)	650	0.49+/-0.01	1.59+/-0.08	67.1%	32.9%	5.18%
X(y scan)	450	0.45+/-0.01	1.56+/-0.08	67.6%	32.4%	3.75%

Table 4: Summary of beam divergence measurement

4.2 Beam Size Measurement

Near field images are analyzed as eight bit bitmap files. To obtain a beam size, a theoretical curve is fit to the intensity profile of the beam waist images. The variance of the fitted curve is used to estimate the RMS beam size within an acceptable range of uncertainty.

4.2.1 Data Preparation

Intensity profiles are obtained by taking a vertical or horizontal line scans across the beam images and recording the pixel values at each position along the line. Figure 27 is an illustration of the line scan process.

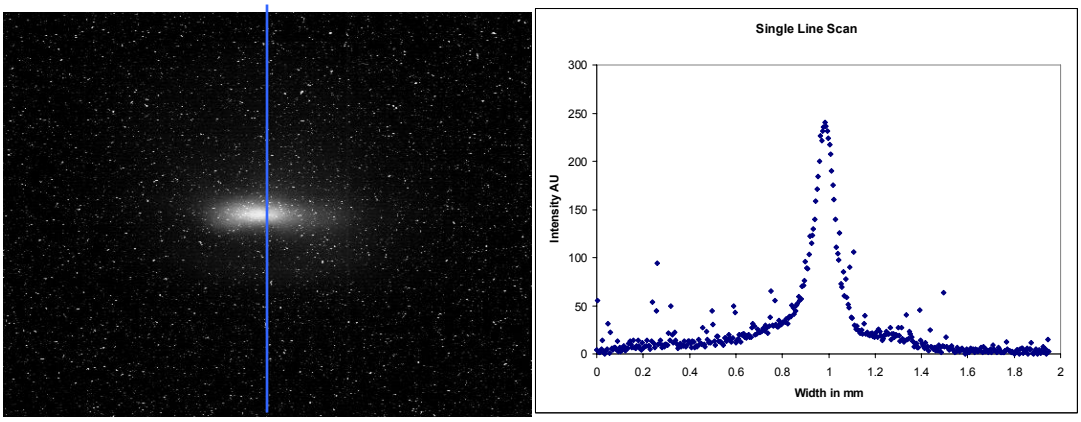

Figure 27: Demonstration of a near field line scan

For each waist condition multiple images of the beam were acquired. Lines scans are taken from each picture at the same location and averaged to reduce error. The uncertainty in the intensity at each pixel value is estimated by calculating the standard deviation from the mean for each intensity value [22]. Figure 28 is a plot of the pixel averaged intensity profile of one of the beam images. The error bars are the calculated standard deviation of the mean for each value.

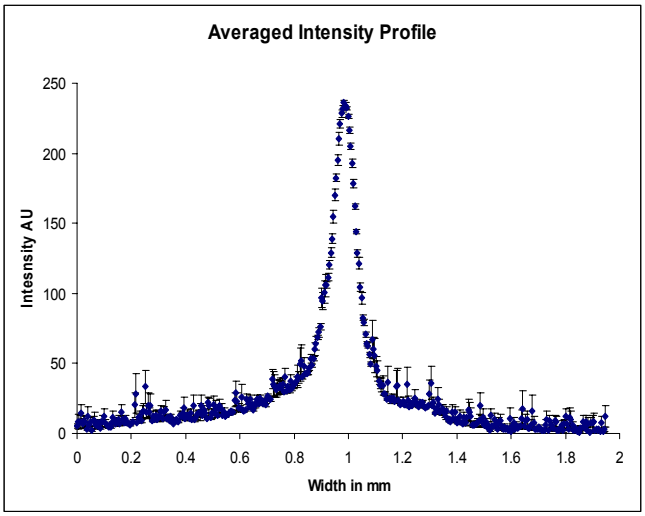

Figure 28: Intensity profile averaged of 10 line scans

At the edges of the distribution, where the intensity is low, the uncertainty is greater due to poorer signal to noise ratio. Despite shielding the camera there is still noise present in the images due to radiation created at the beam dump. The radiation noise can be easily seen in left side of figure 27.

4.2.2 Data Fitting Procedure

Examining the near field images and the associated intensity profiles revealed that throughout all of the images there is a consistent high intensity central peak

surrounded by a well defined low intensity distribution. Figure 29 is an X waist near field image that has been enhanced to highlight the low intensity distribution shown in light blue color.

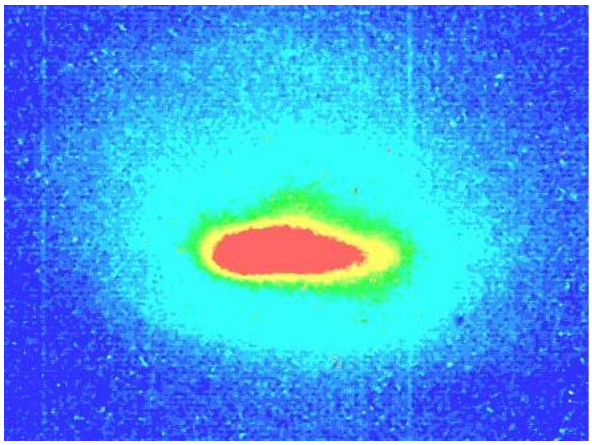

Figure 29: X waist image enhanced to visualize low intensity beam component

Similar to the far field, the near field image also appears to be comprised of two components. In order to measure the RMS size of each component a double Gaussian function was used to fit the intensity profile:

$$I(x) = ae^{-\frac{(x-x_0)^2}{2\sigma_1^2}} + ce^{-\frac{(x-x_1)^2}{2\sigma_2^2}} \qquad (12)$$

where σ_1 and σ_2 are the variance of each of the Gaussian components, x0 is the centroid of the first component, and x1 is the centroid of the second component. The fits are performed using the Sigma plot 10 software package that uses the Marquardt-Levenberg algorithm [23]. Iterations are performed until the sum of the residuals squared is minimized. The software calculates and reports the standard error for each fitted parameter.

4.2.3 Experimental Results for Beam Size Measurements

The following figures show the images of the beam with the location of the line scanned marked on the images and plots of the averaged line scans with the corresponding double Gaussian fit. Also included in the plot of the beam profile is a plot of the individual Gaussian functions that comprise the double Gaussian. For comparison, data for the Y direction of the X waist conditions are presented just as with the far field images in the previous section. Table 5 includes all the fitted parameters of the function in equation 12 and the number of images averaged in each case. During the data collection the same beam focus was used for each wavelength at each waist condition. At the end of the far field data collection for each waist condition a few more near field images were taken just to check for consistency. However, there are inconsistencies in the beam size measurements of these check images. Therefore, the beam size measurements of all the near field images is reported along with the corresponding wavelength of the far field data taken at the time closest to when the near field images were taken. The inconsistency in some of the beam sizes is discussed in the next chapter.

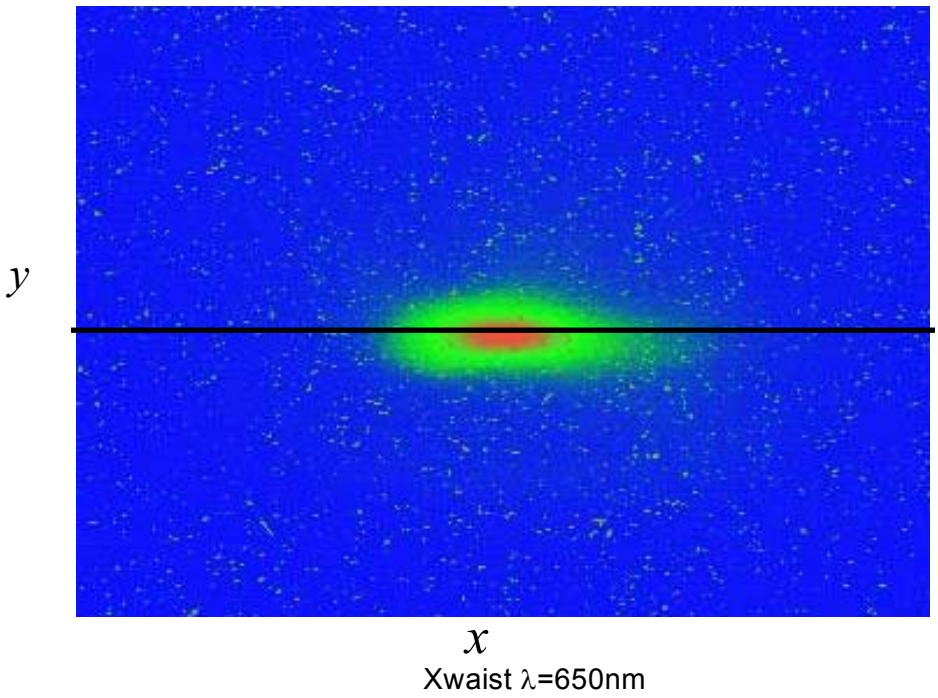

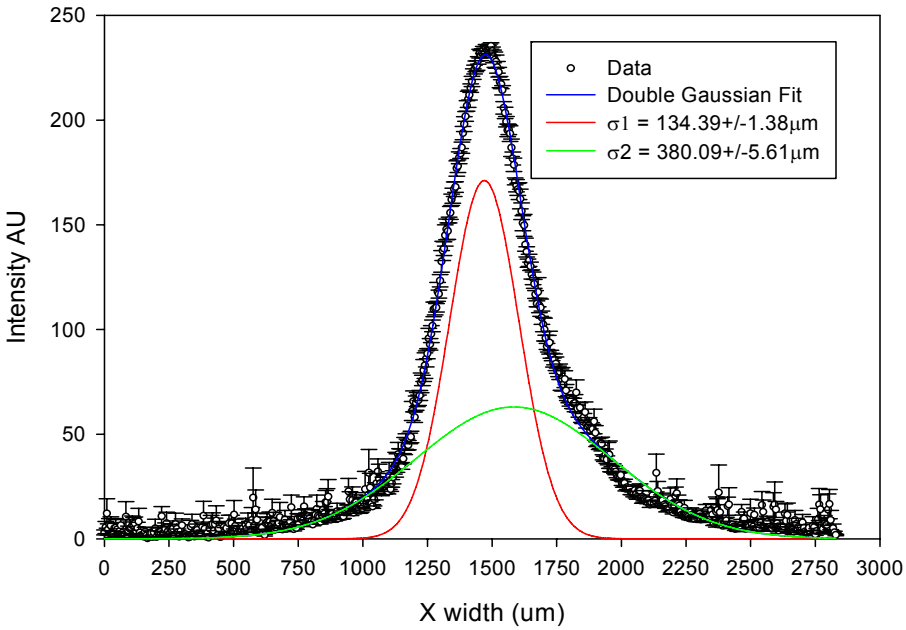

Figure 30: X beam size measurement at an X waist (λ= 650nm)

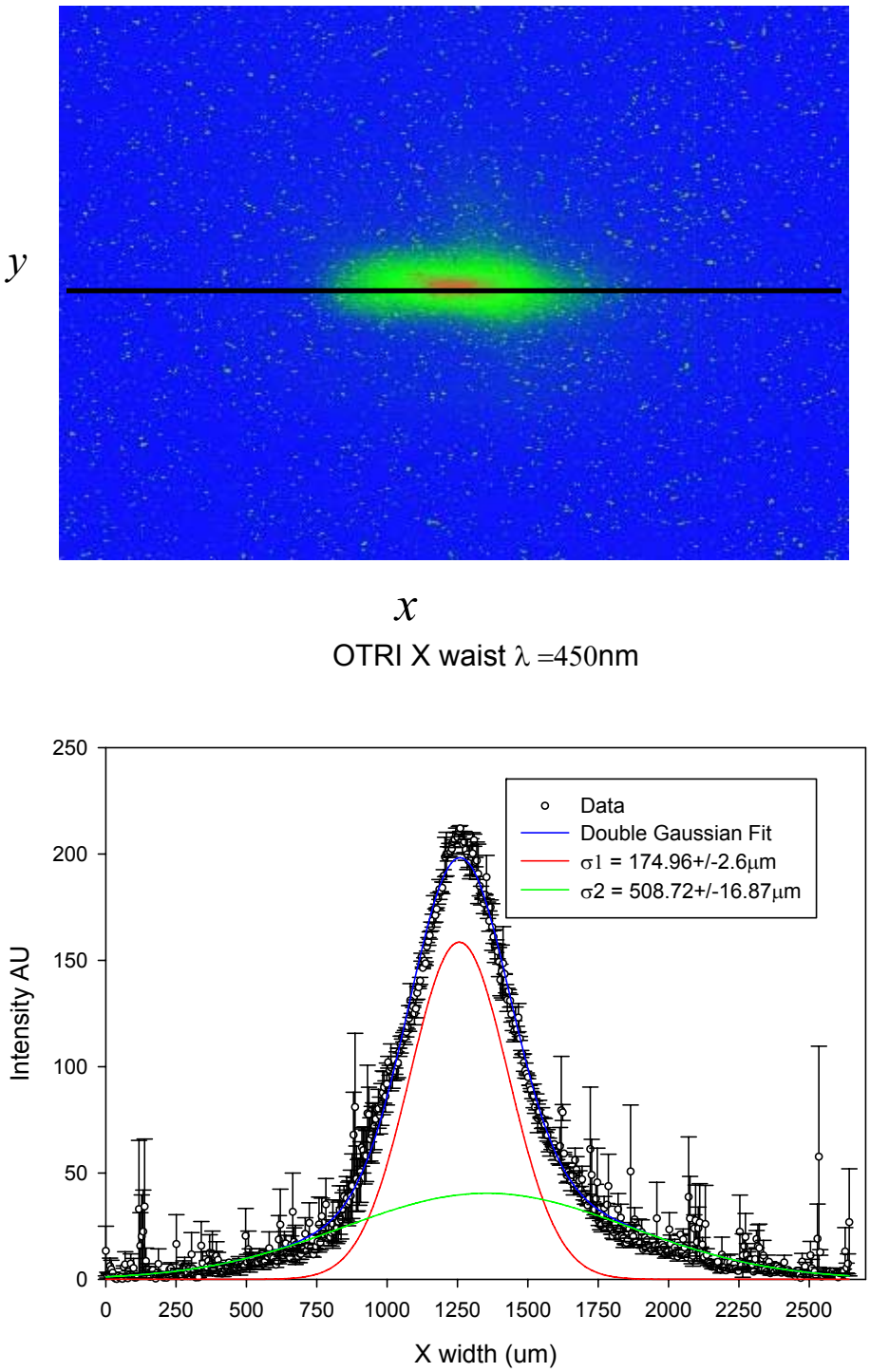

Figure 31: X beam size measurement at an X waist (λ= 450nm)

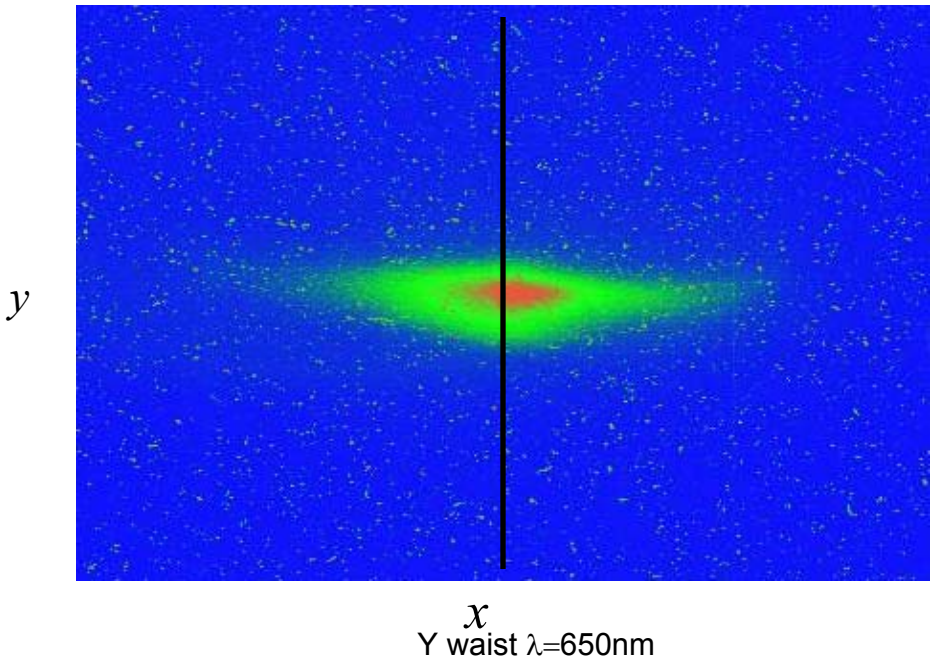

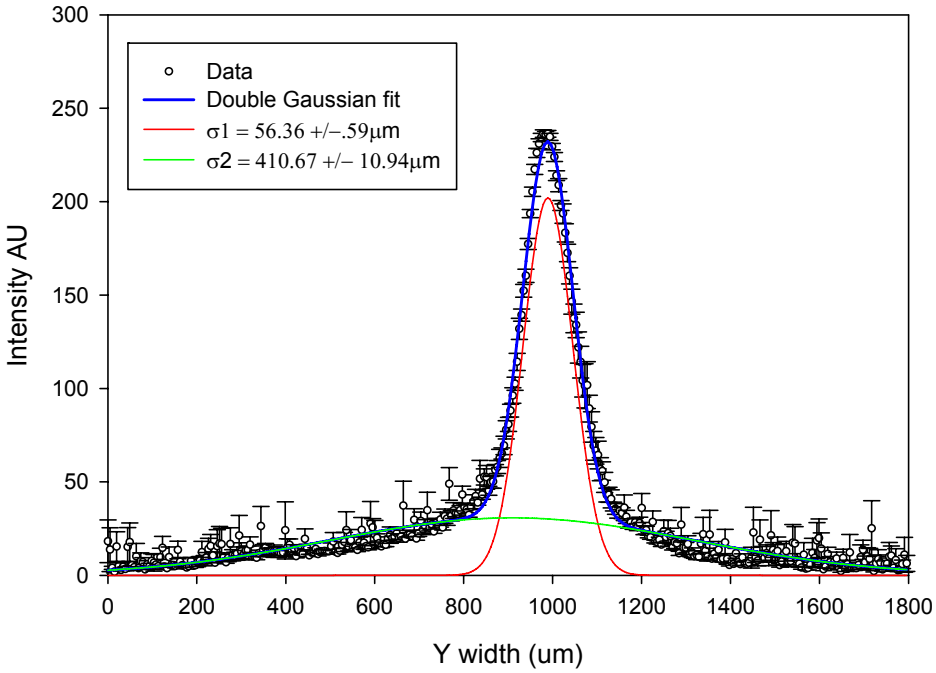

Figure 32: Y beam size measurement at an Y waist (λ= 650nm)

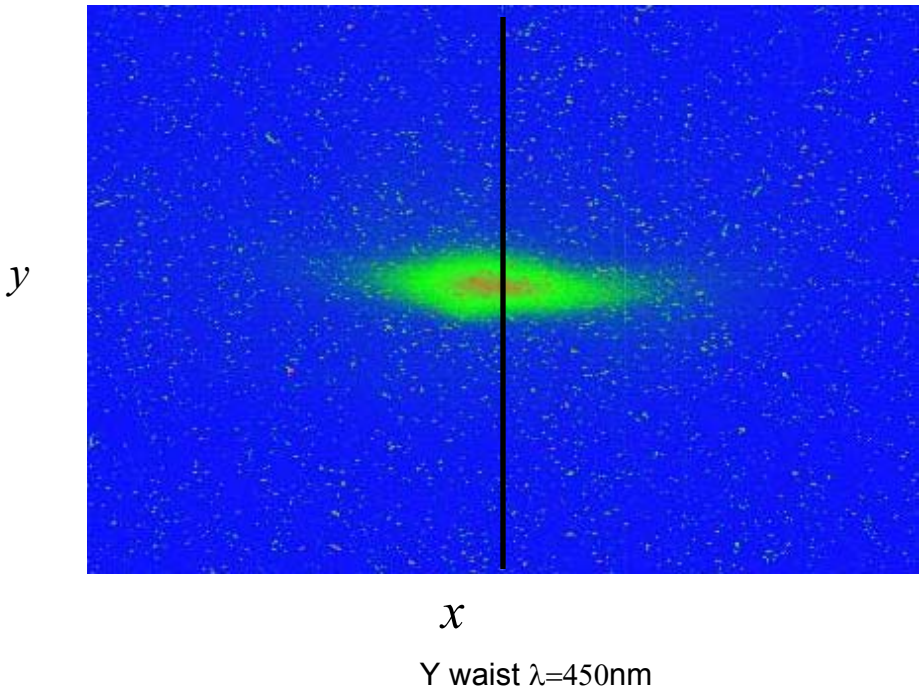

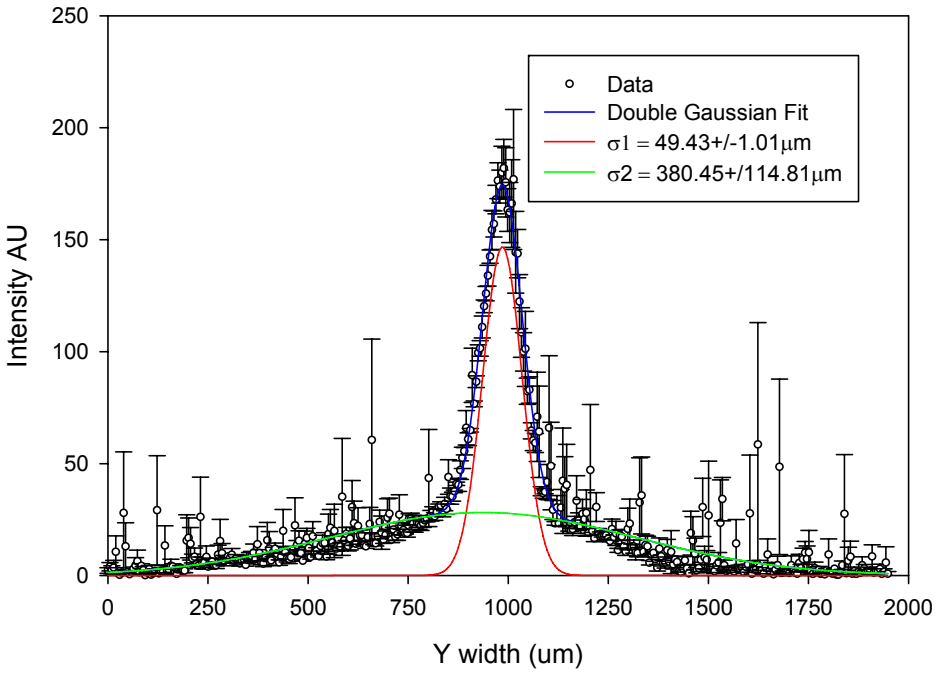

Figure 33: Y beam size measurement at an Y waist (λ= 450nm)

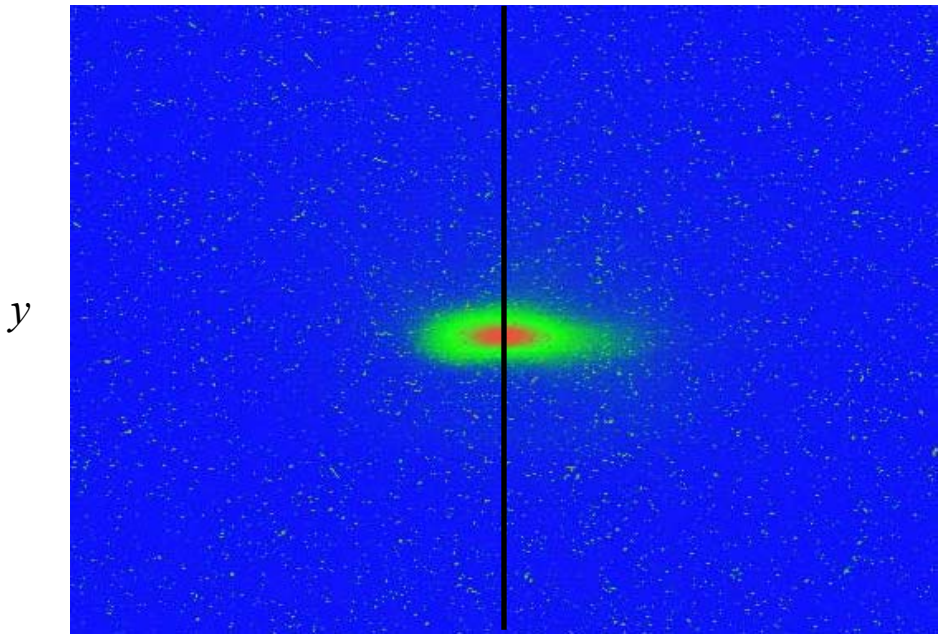

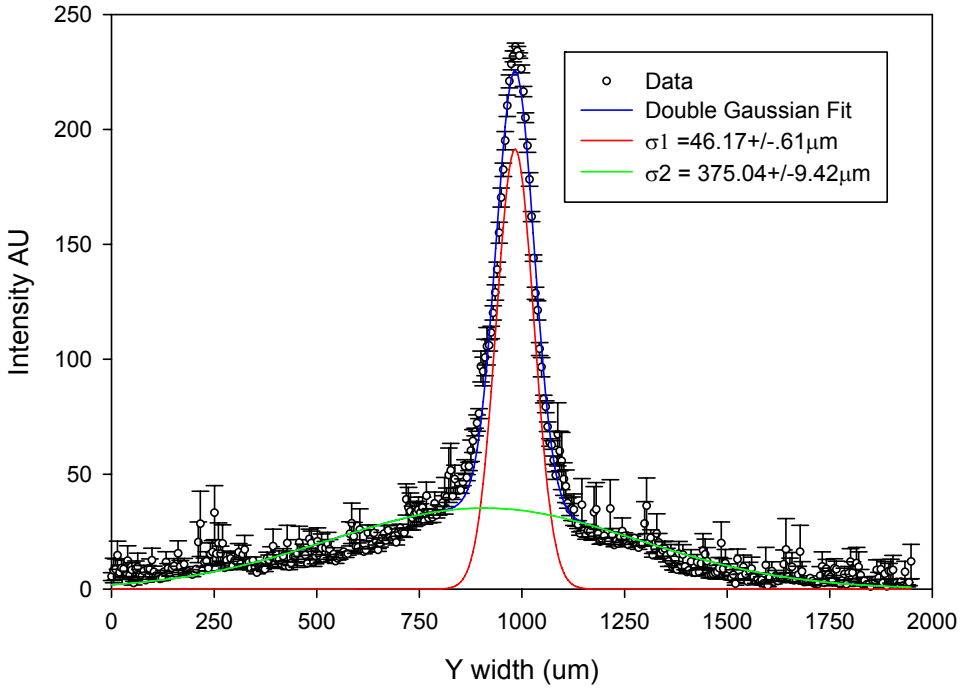

Figure 34: Y beam size measurement at an X waist (λ= 650nm)

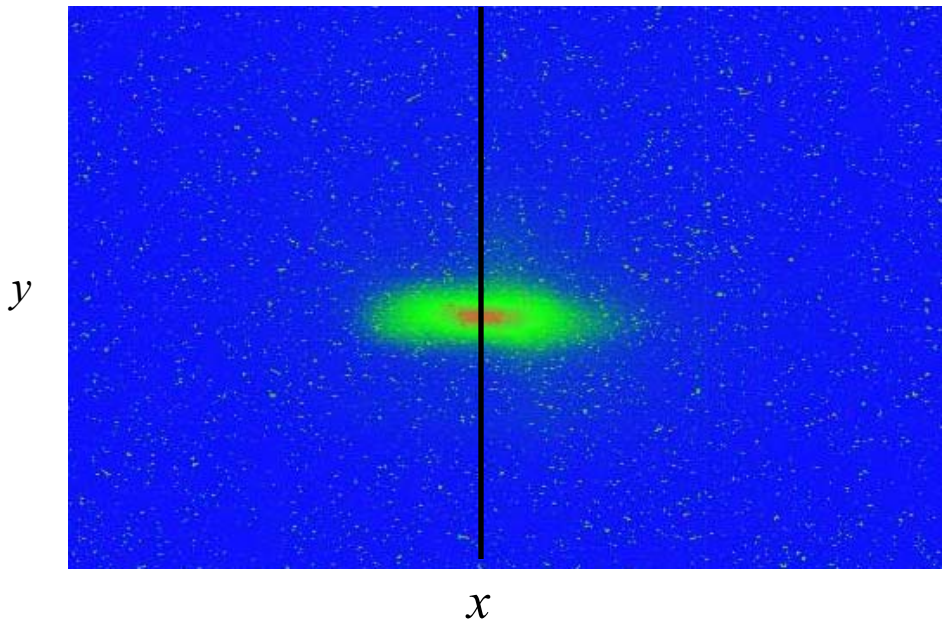

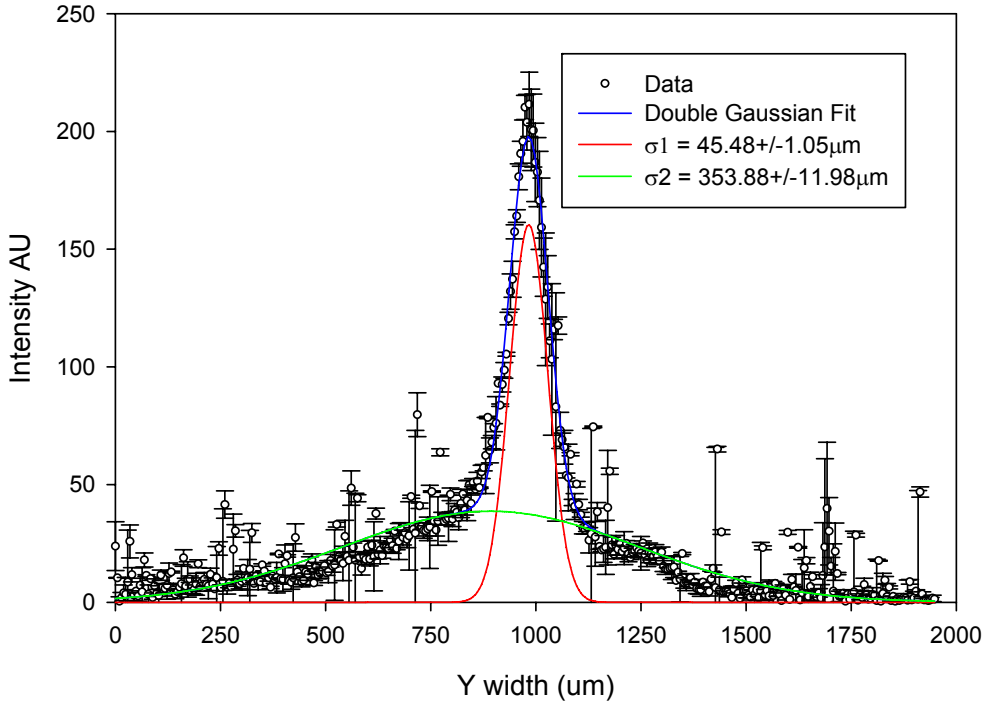

Figure 35: Y beam size measurement at an X waist (λ= 450nm)

Waist	λ (nm)	σ1 (μm)	σ2(μm)	A	c	x0(mm)	x1(mm)	# of pictures averaged
Y	650	56.36+/-.59	410.67+/-10.95	171.08+/-1.80	62.97+/-1.78	1.469	1.584	10
Y	450	49.43+/-1.01	380.45+/-14.81	158.52+/-2.47	40.46+/-2.48	1.25	1.35	3
X	650	134.39+/-1.38	380.09+/-5.61	202.01+/-1.69	30.71+/-0.86	.989	.908+/-.009	10
X	450	174.96+/-2.6	508.72+/-16.87	146.72+/-2.41	28.11+/-1.18	.985	936+/-.012	2
X (y scan)	650	46.17+/-.61	375.04+/-9.42	191.45+/-2.03	35.21+/-0.93	.983	.907+/-.008	10
X (y scan)	450	45.48+/-1.05	353.82+/-11.98	160.37+/-2.99	38.64+/-1.40	.983	.892+/-011	2

Table 5: Summary of results of beam size measurements

Chapter 5: Analysis and Conclusions

5.1 Core - Halo Model

The results of the measurements and observations of both sets of data, *i.e.* near field beam images and far field angular distribution images, suggest that there is a core beam surrounded by a low intensity distributed halo of particles. Such extended low density particle distributions surrounding the core beam have been observed by others [9]. The dynamics of beam halo is of great interest because the presence of halo particles may have adverse effects such as beam loss, gas evolution, and radiation from collisions with the accelerator walls [24]. As shown in the beam images presented in the previous chapter, there is a well defined distribution of particles surrounding the far more intense core of the beam. A similar double distribution has been observed in a proton beam in a beam halo study by Wangler *et al* [25].

The use of the double Gaussian fit on the near field images provides a simple means to estimate the size of the beam core and halo separately. The core and halo components may be offset from one another in the transverse plane. Therefore, when a line scan is taken, the position of the line may not be at the center of both distributions, which could result in some inaccuracy beam size estimate for one of the components if the offset is significant. A two dimensional approach, similar to the two dimensional Gaussian method used to measure the beam divergence, could compensate for an offset of the center of the core and the center of the halo.

As for the far field, none of the theoretical fits could have been made without the presence of a second component. By associating each component of the divergence with either the core or the halo, the divergence and beam size measurements can be combined to estimate the emittance of the core and halo separately.

5.2 Emittance Estimation of the Core and Halo Components

5.2.1 Uncertainty of the Waist Condition

During the experimental run each waist conditioned was focused by adjusting quadrupole magnets till the beam was minimized in either the horizontal (x) or vertical (y) directions. However, using the naked eye to focus to a minimum does not guarantee the beam is focused to a true waist condition. Also, if core and halo are treated as two separate beams, their individual waist conditions in general will not occur at the same focus. Therefore the calculated emittances for each component may not be exact.

The measurements are still very useful because they can be used to provide an upper bound on the emittance of each component. OTRI measures the total divergence of the beam at the interferometer. As discussed in chapter 2, the correlation term of the RMS emittance is zero if the beam is at a true waist. However, if the beam is not truly at a waist the measured beam size will be larger than the beam waist, since the beam waist is the minimum beam size for a given focus in the free drift region after a focusing magnet. The measured beam size can be considered an

upper bound, and the emittances calculated from the product of the measured divergence and size represents upper bounds as well.

5.2.2 Emittance Calculation

The following chart is a summary of emittance calculations of the core and halo using beam divergences and beam sizes for each waist condition and wavelength presented in table 4 and table 5. As discussed in the preceding section, these emittances are best characterized as upper bounds. The Y emittance from the X waist is also presented for comparison to the Y waist emittance as with divergence and beam size measurements in the previous chapter.

Waist	λ	Core emittance (mm-mrad)	Halo emittance (mm-mrad)
X	650nm	13 +/-.43	117.2 +/- 7.72
X	450nm	17.7+/-.66	146.5 +/- 14.02
X (y scan)	650nm	5.1 +/-.17	134.2 +/- 10.11
X (y scan)	450nm	4.6 +/-.21	124.2 +/-10.57
Y	650nm	6.8 +/-.2	212.5 +/- 14.89
Y	450nm	6.0 +/-.23	205.4 +/- 14.85

Table 6: Emittance calculations of core and halo components

An assumption made in the above calculations is that the lower divergence component belongs to the core beam size and that the higher divergence component belongs to the halo beam size. Although it cannot be said that the assumption is correct with 100 % certainty, the assumption is reasonable since the electrons in the core would have to be of a low divergence to be able to focus to small beam sizes.

5.2.3 Inconstancy in X Waist Beam Size

The fitted results are fairly consistent for all of the parameters except one. There is a significant difference between the 650nm and 450nm X waist core and halo beam size measurements. The 10 beam images for the X waist were taken just before the 650nm far field images were taken. The beam focus did not change when taking data for the 450nm far field images. After taking all far field data, two more beam images were taken to check for consistency. Those two images show that beam shape changed over the approximately 30 minutes that the X waist was maintained. The last two beam images taken correspond in time to when the 450nm far field images were taken. Therefore, the beam size measured with the last two beam images is paired with the 450nm far field data.

The reason for the change in the beam is not clear. The divergences measured at each wavelength agree despite the change in beam size. One explanation is there may have been some emittance growth in the system over the data acquisition period. Also, possible unknown systematic error in beam imaging system cannot be ruled out.

5.2.4 Accounting for Scattering

To produce an accurate value for the beam divergence, the divergence resulting from scattering in the front foil of the OTR interferometer must be negligible. However**,** calculating the RMS scattering angle for the front very thin (0.7 microns) aluminum foil used in this experiment is difficult and beyond the scope of this thesis. In a previous experiment under very similar experimental conditions, an approximate RMS scattering angle was estimated to be ~ 0.1 mrad for a 95 MeV electron beam for aluminum foil thickness of 0.7 microns, which was used to measure

the divergence of the NPS linac [26]. The same foil thickness is used in the Jefferson lab experiment. The RMS scattering angle is inversely proportional to the beam energy [12], so for the Jefferson Lab 115 MeV beam the RMS scattering angle should be smaller.

Therefore, a scattering angle of 0.1 mrad is a useful upper bound on RMS scattering angle for the Jefferson Lab to estimate the effect of scattering on the divergence measurements. Assuming Gaussian distributions, the RMS divergence of the beam and the RMS scattering angle add in quadrature [26]. The smallest divergence measured of the Jefferson lab beam during the experimental run is 0.43 mrad. Taking into account the scattering angle the divergence is 0.418 mrad, which is within the uncertainty (0.01) of the measured value of 0.43. Larger measured values of the divergence will be less affected by scattering. So the effect of scattering in the first foil of the OTRI can be reasonable neglected in the divergence measurements presented here.

5.3 Future Work

5.3.1 Determination of the Beam Waist

In work presented above, the waist condition for each transverse component was obtained by visually detecting the smallest focus of the beam from the near field camera feed. Using this method does no guarantee the beam is at a waist condition and is the reason that only upper bounds could be placed on emittance measurements. To better determine the waist condition several beam images can be taken as the focusing magnets focus the beam through a waist at the position of the interferometer

in the beam line. Calculating the beam size in each image and plotting it as a function focusing strength of the magnet will yield a parabolic shaped curve. The minimum of this curve should tell the focusing strength of the magnet that corresponds to the beam waist.

5.3.2 Confirming the Halo-Core Model

To confirm the core halo model assumed in this work, an optical mask can be used in an intermediate image plane to block the light from the core component from reaching the far field camera. The divergence measured from the remaining light can then be used to calculate the divergence of the halo portion of the beam. The results can be compared to the two components measured from the interference pattern created by the whole beam. This procedure would determine if the two components of the divergence measured from the whole beam are indeed attributed to the spatial distributions assumed in this work. The same procedure can also be done masking the halo portion. This experiment is important because is would determine if OTRI is a valuable tool in beam halo studies.

5.3.3 Optical Phase Space Mapping

Optical phase space mapping involves the use of OTRI and an optical mask to segregate light from a particular part of the OTR beam image. The concept is completely analogous to the pepper pot technique used to map the phase space [26]. As described in chapter 3, there is an intermediate ten times magnified image designed into the optical system. Magnifying the beam images will allow for many data points to be recorded from the beam profile using a 1 mm pinhole mask. The

light from that beam image has a direct correspondence to electrons that created it at the interferometer. In other words the light from a particular part of the beam image carries with it information about the electrons from the corresponding position in the actual electron beam. Using small pinhole to mask the light at the beam image, the local divergences of the electron beam corresponding to the pinhole location can be measured by analyzing the interference pattern from the light that passes through the hole to the far field camera. The centroid shift of the OTRI pattern for each beamlet measures the average change in direction for a given beam cross section [27]. The divergence and the centroid shift registered to a particular place in the beam image can then be used to construct a phase space map of the electron beam. The plan is to use a 1 mm pinhole at the magnified beam image site and try to collect at least 10 data points from the beam profile.

Bibliography

[1] I.M. Frank and V.L. Ginsburg, *J. Phys*., vol. 9 (1945) p 353.

[2] P. Goldsmith and J.V. Jelley,"Optical Transition Radiation from Protons Entering Metal Surfaces", *Philosophical Magazine*, vol 4, p 836, 1959.

[3] Aiken *et al.*, "Transition Radiation in Cherenkov Detectors", *Proc. Phys. Soc*., vol. 82, p 710, 1963.

[4] L. Wartski: Doctoral Thesis, Universite de Paris-Sud, Centre d'Orseay, 1976.

[5] L. Wartski, *et al.*, "Interference Phenomenon in Optical Transition Radiation and Its Application to Particle Beam Diagnostics and Multiple Scattering Measurements", *Journal of Applied Physics*, vol. 46, no. 8, p3644, 1975.

[6] R.B. Fiorito and D.W Rule, Ed. Robert E. Shafer , "Optical Transition Radiation Beam Emittance Diagnostics", *Beam Instrumentation Workshop Conference Proceedings*, no. 319, p 21.

[7] A.G. Shkvarunets, R.B. Fiorito, and P.G. O'Shea, "Optical Diffraction-Transition Radiation Interferometry and Its Application to the Measurement of Beam Divergence", *Nuclear Instruments and Methods in Physics Research B,* vol. 201, p 153 , 2003.

[8] R.B. Fiorito, *et al.*, "Interference of Diffraction and Transition Radiation and Its Application as a Beam Divergence Diagnostic", *Physical Review Special Topics-Accelerators and Beams*, vol. 9, no. 052802, 2006.

[9] R.L. Gluckstern, "Analytics Model for Halo Formation in High Current Ion Linacs", *Physical Review Letters*, vol. 73, no. 9, p 1247, 1994.

[10] P.G. O'Shea and J.B. Murphy, "Free Electron Lasers and Synchrotron Light Sources", Internal Publication: Institute for Research in Electronics and Applied Physics, University of Maryland.

[11] Jefferson Lab website: http//www.jlab.org/FEL/

[12] J.D. Jackson, *Classical Electrodynamics*, Hoboken NJ: John Wiley & Sons Inc., 1999.

[13] D.W. Rule and R.B. Fiorito, "The use of Transition Radiation as a Diagnostic for Intense Beams", *Naval Surface Warfare Center TR84-134,* 1984.

[14] C.A. Brau, *Modern Problems in Classical Electrodynamics* , New York, NY: Oxford University Press, 2004

[15] R.B. Fiorito and A.G Shkvarunets, "Use of Optical Transition Radiation Interferometry for Energy Spread and Divergence Measurements", *DIPAC Conference Proceedings,* p 89, 2003

[16] Private Communications with A.G. Shkvarunets

[17] M. Reiser, *Theory and Design of Charged Particle Beams,* New York, NY: John Wiley & Sons Inc, 1994.

[18] Hecht E., *Optics*, San Francisco, CA: Addison Wesley, 2002.

[19] Davis C.C., *Laser and Electro-Optics, Fundamentals and Engineering*, United Kingdom: Cambridge University Press, 1996.

[20] Private Communication with D. Douglas (Jefferson Lab Staff Scientist).

[21] Maxim DL Advanced CCD Imaging Software User Manual.

[22] J.R. Taylor, *An Introduction to Error Analysis*, Sausalito CA: University Science Books, 1997.

[23] Sigma Plot 10 Software Package User Manual.

[24] C.K. Allan, *et al.*, "Beam-Halo Measurements in High-Current Proton Beams", *Physical Review Letters*, vol. 73, no. 9, p 214802-1.

[25] T.P. Wangler, *et al.*, "Particle-Core Model for Transverse Dynamics of Halo", *Physical Review Special Topics – Accelerators and Beams*, vol. 1, p 084201-1, 1998.

[26] R.B. Fiorito, *et al.*, Ed. G.A. Smith and T. Russo "Optical Methods for Mapping the Transverse Phase Space of a Charged Particle Beam", *Beam Instrumentation Workshop Conference Proceedings*, p 187, 2002.

[27] G.P. Le Sage, *et al.*, "Transverse Phase Space Mapping of Relativistic Electron Beams using Transition Radiation", *Physical Review Special Topics – Accelerators and Beams*, vol. 2, p122802-1, 1999.